Accelerating fatigue simulations of a phase-field damage model for rubber

Pascal J. Loew[a,b,*], Leong H. Poh[c], Bernhard Peters[a], Lars A.A. Beex[a]

[a] *Faculty of Science, Technology and Medicine, University of Luxembourg, Luxembourg*
[b] *SISTO Armaturen S.A., Echternach, Luxembourg*
[c] *Department of Civil and Environmental Engineering, National University of Singapore, Singapore*

Abstract

Phase-field damage models are able to describe crack nucleation as well as crack propagation and coalescence without additional technicalities, because cracks are treated in a continuous, spatially finite manner. Previously, we have developed a phase-field model to capture the rate-dependent failure of rubber, and we have further enhanced it to describe failure due to cyclic loading. Although the model accurately describes fatigue failure, the associated cyclic simulations are slow. Therefore, this contribution presents an acceleration scheme for cyclic simulations of our previously introduced phase-field damage model so that the simulation speed is increased to facilitate large-scale simulations of industrially relevant problems. We formulate an explicit and an implicit cycle jump method, which, depending on the selected jump size, reduce the calculation time up to 99.5%. To circumvent the manual tuning of the jump size, we also present an adaptive jump size selection procedure. Thanks to the implicit adaptive scheme, all material parameters are identified from experiments, which include fatigue crack nucleation and crack growth. Finally, the model and its parameters are validated with additional measurements of the fatigue crack growth rate.
© 2020 Elsevier B.V. All rights reserved.

1. Introduction

Numerous structural components and applications are subjected to cyclic loading. Accurate simulations to identify the cycle-to-failure number not only reveal the best design but also reduce maintenance efforts and associated costs. Fatigue simulations require both a failure model able to accumulate damage due to repetitive loading and fast solution strategies for cyclic loading [1].

Treating cracks in a continuous manner with a finite damage zone controlled by a length scale parameter, phase-field damage models are able to handle effortless topological complex cracks. They do not require additional enhancements to describe crack nucleation, branching and crack coalescence [2–4], and the location of cracks needs not to be known in advance, as for instance with standard cohesive zone models [5–8]. We want to note that coupling

---

the extended finite element method (XFEM, [9–11]) with a cohesive zone model can deal with cracks not known in advance [12].

Phase-field models are similar to gradient-enhanced damage models [13–15], as both rely on a length scale parameter to obtain mesh independent results [16–18]. Miehe and Schänzel [19] were the first to extend phase-field damage models to finite strains and rubber, while its extension to rate-dependency, with experimental identification and validations can be found in [20]. The ability to represent complex crack patterns and coalescence was highlighted by Wu et al. [21], who applied the method to carbon black reinforced rubber. San and Waisman [22] and Russ and Waisman [23] are other examples in which phase-field damage models were applied — particularly to optimize structural designs.

Focusing on cyclic loading, Amendola et al. [24] presented a fatigue phase-field damage model by introducing a fatigue history variable in the Ginzburg–Landau equation. Caputo and Fabrizio [25] also considered an accumulation of damage dependent on the time and the environment (i.e. aging). Boldrini et al. [26] equipped a phase-field damage model for fatigue with temperature effects due to the load cycles. Alessi et al. [27] presented a different approach, which reduces the fracture toughness with an increase of the load cycle. While Alessi et al. [27] focused exclusively on one-dimensional examples, Carrara et al. [28] and Mesgarnejad et al. [29] proposed similar models for two- and three-dimensional multi-crack configurations. Lo et al. [30] defined viscous damage dissipation so that crack growth under cyclic loading occurs. Loew et al. [1] presented a model for finite strains and validated two-dimensional simulations with experimental results.

Many contributions focus on the acceleration of phase-field fracture simulations. Heister et al. [31] proposed adaptive mesh refinement schemes, Cheng et al. [32] introduced a wavelet-enriched adaptive hierarchical framework and Patil et al. [33] combined phase-field damage modeling with XFEM. All three works shorten the computing time, since a fine mesh is only required in the vicinity of the crack. Another possibility is to use a monotonic solver, so that the elaborate iterations in the conventionally applied staggered scheme [2,34] between the coupled damage-displacement equations are avoided [35]. Although all these methods reduce the computational effort, the application to cyclic loading is still not practical, since every load cycle must be fully simulated.

The aim of this contribution is, therefore, to redevelop explicit and implicit cycle jump schemes from literature for fatigue phase-field simulations. We adopt the acceleration scheme for our earlier fatigue phase-field model of [1], modified here to incorporate a new fatigue damage source.

The first cycle jump scheme was introduced for continuum damage models by Van Paepegem et al. [36] to extrapolate the stiffness degradation of composites. Turon et al. [37] used this idea to simulate high cycle delamination with cohesive elements and Cojocaru et al. [38] extrapolated both the amount of damage as well as other state variables. Peerlings et al. [39] introduced a predictor–corrector cycle jump scheme for high-cycle fatigue to enable large cycle jumps. Decomposing the problem into slow (averaged) and fast (oscillation inside a load cycle) time components, two time-scale asymptotic time integration for fatigue problems was presented by Oskay and Fish [40], which Heczko and Kottner [41] applied to elastomeric materials. Since this multi time-scale approach requires the solution of two subproblems at each time-step, the speed may not be much improved compared to that of single time-scale calculation [42].

Joseph et al. [43] proposed a wavelet-based transformation with an implicit cycle jump scheme. In contrast to standard finite element simulations of solids, the wavelet framework does not solve for the nodal displacements at each time increment, but for the coefficients of the wavelets, which form the nodal displacements at all time instances for one load cycle. Comparing a standard finite element implementation to the wavelet-based implementation of Joseph et al. [43], both using an implicit cycle jump scheme, Beusink [44] showed that most of the speed up is related to the implicit scheme and not the wavelet transformation. Accordingly, we focus only on cycle jump schemes in this work.

Besides the main aim of proposing explicit and implicit cycle jump schemes to accelerate fatigue phase-field simulations, this contribution contains three additional novelties:

- A new (rate-independent) fatigue damage source is introduced in the framework of Loew et al. [1], which prohibits fatigue crack growth due to compressive stresses.
- Identification and validation experiments, including crack nucleation and growth, are presented.
- An adaptive jump size procedure is formulated for the implicit scheme in order to circumvent the need for manual tuning of the step size for cycle jumps.
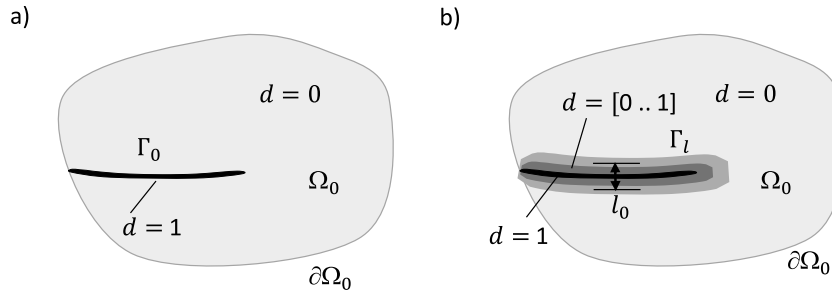
Fig. 1. Fatigue phase-field damage model in 2D: A sharp crack Γ_0 (a) is approximated with a crack surface Γ_l (b). The length scale l_0 controls the width of the process zone.

The paper is organized as follows. In Section 2, we present the fatigue phase-field damage model for rubber. Following, we introduce the explicit and implicit cycle jump schemes to accelerate the calculations in Section 3, and demonstrate the performance of both schemes in Section 4. Section 5 presents the experimental validation and we conclude the contribution in Section 6.

We denote scalars with lowercase and capital letters (a and A). Vectors are written in bold ($\mathbf{a}$, $\mathbf{A}$).

2. Fatigue phase-field damage model

In this section, we present our fatigue phase-field damage model. Damage (i.e. cracks) is described with a scalar variable $d \in [0, 1]$ so that $d = 1$ on an internal discontinuity Γ_0 and $d = 0$ on $\Omega_0 \setminus \Gamma_0$ (Fig. 1 a)).

We describe the motion and deformation of the body Ω_0 in the reference configuration by displacement $\mathbf{u}$ and deformation gradient $\mathbf{F} = \mathbf{I} + \nabla_0\mathbf{u}$. $\mathbf{I}$ denotes the unit tensor and spatial derivatives associated with the reference configuration are denoted by $\frac{\partial \cdot}{\partial \mathbf{X}} = \nabla_0(\cdot)$. The balance of mechanical energy requires:

$$\dot{E} + \dot{D} - \dot{R} - \dot{P}^{ext} = 0, \tag{1}$$

where $\dot{E}$, $\dot{D}$ and $\dot{P}^{ext}$ denote the internally stored energy, dissipated energy and the externally supplied energy per time unit, respectively. Fatigue damage is, on a pure phenomenological basis, described by fatigue damage source $\dot{R}$ [1]. $\dot{R}$ could also be interpreted as a reduction of $\dot{D}$. That would correspond to recently published fatigue phase-field damage models [27,28] and [29], where a reduction of the dissipated energy is achieved by multiplication with a load history dependent variable. However, we prefer the interpretation of R as the energy of an extrinsic volumetric micro-force (see [45–48] and [49]). According to Frémond and Nedjar [46] such a source of damage can for example be produced by chemical or electrical actions, which break the bonds inside a material. We assume that cyclic loading leads to stress and strain-induced aging processes, i.e. the cross-link density evolves due to chain-scission and cross-linking reactions. Following, microcracks form, merge and cause damage at the macroscale. In this case, extrinsic does not refer to a global external force, but to processes on a different scale.[1] The relations for $\dot{E}$, $\dot{D}$, $\dot{P}^{ext}$ and $\dot{R}$ are presented in the following subsection.

2.1. Rate of internally stored energy

The internally stored energy in the bulk reads:

$$E = \int_{\Omega_0 \setminus \Gamma_0} \psi^{elas} dV, \tag{2}$$

with strain energy density ψ^{elas}.[2] By introducing degradation function $g_d = g_d(d)$, the integration in Eq. (2) can be performed over the entire domain Ω_0:

$$E = \int_{\Omega_0} \left(g_d \psi^{elas} \right) dV. \tag{3}$$

---

[1] This interpretation enables us to imply that the rate of dissipated crack energy is independent of the (fatigue) load history variable h (Eq. (16)). Or in other words, a crack caused by cyclic loading dissipates as much energy as a crack caused by monotonic loading.

[2] Rate-dependent effects could be incorporated by splitting the strain energy density into an elastic and viscous contribution [20].

The degradation function controls the mechanical response with respect to the virgin state and requires:

$$
\begin{aligned}
&g_d(d = 0) = 1 \\
&g_d(d = 1) = 0 \\
&\left.\frac{\partial g_d}{\partial d}\right|_{d=1} = 0.
\end{aligned}
\tag{4}
$$

We use a recently proposed degradation function [50,51]:

$$
g_d = \frac{(1 - d)^2}{(1 - d)^2 + ad(1 - \frac{1}{2}d)},
\tag{5}
$$

where a denotes an additional material parameter. Wu and Nguyen [50] derived from 1D analytical results that the failure strength $f_t \propto (a \cdot l_0)^{-1/2}$. Therefore, by adjusting material parameter a according the value of length scale l_0, the failure strength and the force–displacement responses can be made independent of the length scale [1].

The rate of the internally stored energy then reads:

$$
\dot{E} = \int_{\Omega_0} \left(g_d \frac{\partial \psi^{elas}}{\partial \mathbf{F}} : \dot{\mathbf{F}} + \frac{\partial g_d}{\partial d} \psi^{elas} \dot{d} \right) dV,
\tag{6}
$$

and the elastic strain energy density is defined according to [52]:

$$
\psi^{elas} = \sum_{i=1}^{3} C_i (I_1 - 3)^i,
\tag{7}
$$

where $I_1 = tr(\mathbf{F}^T \cdot \mathbf{F})$ and C_i denote the hyperelastic material parameters. The first Piola–Kirchhoff stress can then be expressed as follows:

$$
\mathbf{P} = \frac{\partial \psi^{elas}}{\partial \mathbf{F}} = 2 \sum_{i=1}^{3} i \; C_i (I_1 - 3)^{(i-1)} \; \mathbf{F}.
\tag{8}
$$

2.2. Rate of dissipation

Since we neglect rate-dependent effect, the rate of dissipation is only attributed to the rate of dissipation due to crack growth:

$$
\dot{D} = \dot{D}^{crack}.
\tag{9}
$$

As the energy dissipated by the formation of a unit crack area is denoted by G_c, the energy dissipated through crack growth is expressed as:

$$
D^{crack} = \int_{\Gamma_0} G_c \, dA.
\tag{10}
$$

The sharp discontinuity Γ_0 is approximated $\Gamma_0 \approx \Gamma_l = \int_{\Omega_0} \gamma_l \, dV$ with crack density function $\gamma_l = \gamma_l(d, l_0)$ [4], which introduces length scale l_0 to control the width of the damage zone (see Fig. 1 b)). Thus, multiplying Eq. (10) with γ_l, we avoid integrating over the fractured surface and change the integration to a volume integral over the domain Ω_0:

$$
D^{crack} = \int_{\Omega_0} G_c \gamma_l \, dV.
\tag{11}
$$

Following [51], we define the crack density function:

$$
\gamma_l = \frac{1}{c_0} \left[\frac{1}{l_0} w + l_0 (\nabla_0 d \cdot \nabla_0 d) \right],
\tag{12}
$$

where w denotes a geometric crack function $w = w(d) \in [0, 1]$ with the constraints $w(d = 0) = 0$ and $w(d = 1) = 1$. c_0 denotes a scaling parameter to ensure $\Gamma_0 = \Gamma_l$ for $l_0 \to 0$. Defining $w = 2d - d^2$ [50], we write $c_0 = 4 \int_0^1 \sqrt{w(\delta)} d\delta = \pi$.

By differentiating with respect to time, the dissipation rate due to crack formation reads:

$$\dot{D}^{crack} = \int_{\Omega_0} G_c \frac{1}{\pi} \left(\frac{1}{l_0} (2 - 2d) \dot{d} + 2l_0 \nabla_0 d \cdot \nabla_0 \dot{d} \right) dV. \tag{13}$$

The second law of thermodynamics requires:

$$\dot{D} = \dot{D}^{crack} \geq 0, \tag{14}$$

which is fulfilled by imposing constraint $\dot{d} \geq 0$ [20].

2.3. Rate of externally applied energy

By denoting the surface traction and volumetric body force vector $\mathbf{t}_0$ and $\mathbf{b}_0$, the rate of externally applied energy is:

$$\dot{P}^{ext} = \int_{\partial \Omega_0} \mathbf{t}_0 \cdot \dot{\mathbf{u}} \, dA + \int_{\Omega_0} \mathbf{b}_0 \cdot \dot{\mathbf{u}} \, dV. \tag{15}$$

2.4. Fatigue damage source

First, we introduce $h = h(t)$, an accumulated history variable, which cannot decrease:

$$\dot{h} \geq 0. \tag{16}$$

h is defined later but basically any scalar quantity, which is able to describe fatigue loads, may be used. The energetic contribution of fatigue damage reads:

$$R = \int_{\Omega_0} \int_T g_f \zeta_d h^{\zeta_e} \dot{d} \, dt \, dV, \tag{17}$$

where g_f denotes a fatigue degradation function, and ζ_d and ζ_e two fatigue material parameters. Fatigue failure of rubbers can often be described with a power law (see Figs. 16, 20 and 23), so that the formulation in Eq. (17) appears natural. The influence of these material parameters is presented in Appendix A. Note that this is a purely phenomenological formulation, primarily based on macroscopic experimental observations. "Work" is only performed when damage grows, so $\dot{d}$ is included. It is also worth mentioning that R is a process-dependent variable and not a state function.

A load history $h = h(t, \epsilon)$ with ϵ denoting the strain was presented by Alessi et al. [27]. However, Carrara et al. [28] demonstrated that this leads to mesh dependent results because of strain singularities at crack tips and proposed instead an energetic formulation. In our rate-dependent framework [1], promising results were achieved by basing $h = h(t, D^{visc})$ on the viscous dissipation of the bulk D^{visc}.

Departing from [1], we neglect rate-dependent effects and propose a load history variable $h = h(t, \psi^{elas})$ depending on the elastic strain energy density $\psi^{elas} = \psi^{elas}(I_1)$.[3] Rate-dependent effects play a major role in fracture of rubber [20,53,54] and for high frequent cyclic loading heat build-up, followed by temperature depending change of the material properties and thermal degradation can be experimentally observed [55,56]. However, Stadlbauer et al. [57] also showed that the influence of the strain rate and the load function (e.g. sine wave or "square" pattern) on the service life in temperature controlled experiments is insignificant. We limit ourselves to relatively low strain-rates to ensure temperature constancy in our experiments.

The load history is:

$$h = \frac{1}{\hat{h}} \int_T s_l s_c \dot{\psi}^{elas} dt, \tag{18}$$

---

[3] $I_1 = tr(\mathbf{F}^T \cdot \mathbf{F})$ is the first invariant of the right Cauchy–Green tensor.

where s_l and s_c denote two switch functions.[4] $\hat{h} = 1$ N/mm^2 denotes a normalization parameter to ensure h is dimensionless. Without this factor, units would not match if material parameter $\zeta_e \neq 1$. The first switch, s_l, ensures that damage growth only occurs due to loading, and not due to unloading:

$$s_l = \begin{cases} 1, & \text{if } \dot{I}_1 \geq 0 \\ 0, & \text{otherwise.} \end{cases} \tag{19}$$

The second switch, s_c, prevents fatigue damage growth due to compressive loading and accelerates fatigue crack growth in regions with a high hydrostatic pressure $p = \frac{1}{3}tr(\mathbf{F}\mathbf{P}^T)$[5]:

$$s_c = \begin{cases} 1 + \zeta_p \cdot \max(p - \zeta_t, 0), & \text{if } p \geq 0 \\ 0, & \text{otherwise.} \end{cases} \tag{20}$$

ζ_p and ζ_t denote two additional fatigue material parameters to be defined. In rubber, (fatigue) cracks tend to nucleate in regions of high hydrostatic pressure [48,60,61] and [62] and we take this effect into account with ζ_t and ζ_p. A demonstration of the characteristics of the new load history h can be found in Appendix B.

Fatigue degradation function $g_f = g_f(d)$ has the following properties:

$$\begin{aligned} g_f(d=0) &= 1 \\ g_f(d=1) &= 0. \end{aligned} \tag{21}$$

It ensures that no work is performed in completely damaged domains. As in [1], we set $g_f = -\frac{\partial g_d}{\partial d}$, where g_d denotes the degradation function of the bulk, see Eq. (5). With this choice, h and ψ^{elas} are similarly reduced with an increase of the damage (see Eq. (26)), leading to a relatively straightforward implementation.

Finally, taking the time derivatives of Eq. (17), the fatigue damage source reads:

$$\dot{R} = \int_{\Omega_0} -\frac{\partial g_d}{\partial d} \zeta_d h^{\zeta_e} \dot{d} \, dV. \tag{22}$$

2.5. Balance of mechanical energy

Inserting Eqs. (6), (9), (15) and (22) into Eq. (1), we obtain:

$$\begin{aligned} &- \int_{\Omega_0} \left(\nabla_0 \cdot \left(g_d \frac{\partial \psi^{elas}}{\partial \mathbf{F}} \right) + \mathbf{b}_0 \right) \cdot \dot{\mathbf{u}} \, dV \\ &+ \int_{\partial \Omega_0} \left(\left(g_d \frac{\partial \psi^{elas}}{\partial \mathbf{F}} \right) \cdot \mathbf{n}_0 - \mathbf{t}_0 \right) \cdot \dot{\mathbf{u}} \, dA \\ &+ \int_{\Omega_0} \left(\frac{\partial g_d}{\partial d} \left(\psi^{elas} + \zeta_d h^{\zeta_e} \right) + \frac{G_c}{l_0 \pi} (2 - 2d) - G_c l_0 \frac{2}{\pi} \nabla_0^2 d \right) \dot{d} \, dV \\ &+ \int_{\partial \Omega_0} G_c l_0 \frac{2}{\pi} \nabla_0 d \cdot \mathbf{n}_0 \dot{d} \, dA = 0. \end{aligned} \tag{23}$$

With the following Neumann boundary conditions:

$$\left(g_d \frac{\partial \psi^{elas}}{\partial \mathbf{F}} \right) \cdot \mathbf{n}_0 = \mathbf{t}_0 \quad \text{and} \quad \nabla_0 d \cdot \mathbf{n}_0 = 0, \tag{24}$$

we extract the governing equation for displacement field $\mathbf{u}$:

$$\nabla_0 \cdot \left(g_d \frac{\partial \psi^{elas}}{\partial \mathbf{F}} \right) + \mathbf{b}_0 = 0, \tag{25}$$

---

[4] A third switch s_n could be additionally introduced to ensure that fatigue damage can only grow when a threshold (ζ_n) is reached:

$$s_n = \begin{cases} 1, & \text{if } I_1 \geq \zeta_n \\ 0, & \text{otherwise.} \end{cases}$$

Gent [58] shows the experimental justification to use such a threshold for rubber, but since we do not have experimental data at these load levels we do not include this third switch.

[5] Definition of p according to [59].

and for damage field d:

$$\frac{\partial g_d}{\partial d}\left(\psi^{elas} + \zeta_d h^{\zeta_e}\right) + \frac{G_c}{l_0\pi}(2-2d) - G_c l_0 \frac{2}{\pi}\nabla_0^2 d = 0. \tag{26}$$

2.6. Tension–compression split

To account for the closing of cracks and to prevent crack growth due to compressive loading [63,64], we split the bulk energy into a positive ψ^+ (tensile) and a negative ψ^- (compression) part [3,65].[6]

(Nearly) incompressible rubbery polymers are described with an elastic strain energy density decomposed into an isochoric and volumetric part [66]:

$$\psi^{elas} = \psi^{iso}(\bar{\mathbf{F}}) + \psi^{vol}(J), \tag{27}$$

where $\bar{\mathbf{F}} = J^{-1/3}\mathbf{F}$ and $J = det(\mathbf{F})$. In case of plane stress situations (which we restrict ourselves to), the incompressibility constraint is generally incorporated via substitution [59], so that $J = 1$, $\psi^{vol} = 0$ and $\psi^{elas} = \psi^{iso}$. Using hydrostatic pressure p to distinguish between compression and tension, we write[7]:

$$\psi^+ = \begin{cases} \psi^{elas}, & \text{if } p \geq 0 \\ 0, & \text{otherwise}, \end{cases}$$
$$\psi^- = \begin{cases} 0, & \text{if } p \geq 0 \\ \psi^{elas}, & \text{otherwise}. \end{cases} \tag{28}$$

Application of this split [3,65] in Eq. (25) and Eq. (26) leads to:

$$\nabla_0 \cdot \left(g_d \frac{\partial \psi^+}{\partial \mathbf{F}} + \frac{\partial \psi^-}{\partial \mathbf{F}}\right) + \mathbf{b}_0 = 0, \tag{29}$$

and:

$$\frac{\partial g_d}{\partial d}\left(\psi^+ + \zeta_d h^{\zeta_e}\right) + \frac{G_c}{l_0\pi}(2-2d) - G_c l_0 \frac{2}{\pi}\nabla_0^2 d = 0. \tag{30}$$

Eqs. (29) and (30) are then transformed into their respective weak form using the standard Galerkin procedure. We discretize the 2D domains under plane stress circumstances with bilinear isoparametric quadrilateral elements. Details on the numerical implementation can be found in [20].

Since we limit ourselves to plane stress applications, practically only thin structures can be simulated. The ability of these structures to absorb compressive stress is low because they buckle quickly in practice. Therefore, a comprehensive study of compressive loads is not realistic and we do not claim that the proposed split is advantageous over recently published works, see e.g. [67] or [68]. Still, we demonstrate in Appendix D that the proposed split successfully avoids crack penetration and crack growth in compression.

In plane stress settings the incompressibility constraint is incorporated by substitution — instead of via (pressure) fields of Lagrange multipliers for perfect incompressibility, or via penalty terms for near incompressibility. Therefore, the standard volumetric deformation based split [65] is not applicable since $J = 1$ and we do not need to compute the spectral decomposition of the strain tensor [3].

3. Explicit and implicit cycle scale time integration

Lifetime predictions are accelerated thanks to explicit [36,37] or implicit [43,44] cycle jump scheme. The basic idea is to simulate a few cycles, and then extrapolate the results for $\mathbf{u}$, d and h over a selected interval. Note that we do not only extrapolate the damage variable but all relevant variables [37,69,70]. While the explicit extrapolation is solely based on past results, in the implicit scheme the values after the cycle jump are also considered. The implicit procedure is therefore comparable to an explicit procedure with a predictor–corrector step [39].

---

[6] Switch s_c (Eq. (20)) prohibits fatigue crack growth in compression. The split of the energy does not stop h from growing because $h = h(\psi^{elas})$.

[7] For the present manuscript, we limit ourselves to incompressible materials in plane stress situations and the material model of Yeoh [52]. The boundary conditions $P_{33} = 0$ and $J = 1$ enable the direct calculation of $p = 2\frac{\partial\psi^{elas}}{\partial I_1}(\frac{1}{3}I_1 - F_{33}^2)$ (see [59] for details). Since $\frac{\partial\psi^{elas}}{\partial I_1} \geq 0$, the split could equally depend on the deformation measure $(\frac{1}{3}I_1 - F_{33}^2)$.
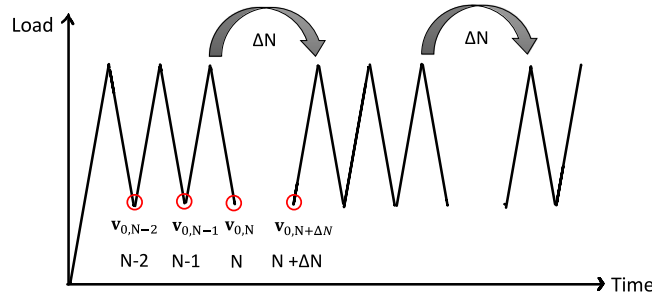
Fig. 2. Explicit cycle jump scheme.

Depending on the extrapolation scheme and the non-linearity of the structural response, the jump size $\Delta N = 1..10..10^6$ is fixed. The process of alternating between calculations and jumping of cycles is repeated until the lifetime of the component is reached.

This procedure reduces the number of simulated load cycles and consequently the total calculation time. First, we present the explicit scheme and compare it with the implicit scheme. Based on the first results in Section 4.1, we propose in Section 3.2.2 an adaptive step size procedure. To ease the notation below, we store $\mathbf{u}$, d (both nodal values) and h (computed at the integration points) in $\mathbf{v}$.

3.1. Explicit cycle scale time integration

We extrapolate the evolution of variable $\mathbf{v}_{0,N}$ over a discrete number of load cycles ΔN with a second order Taylor series (see Fig. 2). The index 0 indicates the start of a load cycle:

$$\mathbf{v}_{0,N+\Delta N} = \mathbf{v}_{0,N} + \Delta N \left.\frac{\partial \mathbf{v}_0}{\partial N}\right|_N + \frac{1}{2}\Delta N^2 \left.\frac{\partial^2 \mathbf{v}_0}{\partial N \partial N}\right|_N, \tag{31}$$

with

$$\left.\frac{\partial \mathbf{v}_0}{\partial N}\right|_N = \mathbf{v}_{0,N} - \mathbf{v}_{0,N-1}, \tag{32}$$

and

$$\begin{aligned} \left.\frac{\partial^2 \mathbf{v}_0}{\partial N \partial N}\right|_N &= \left.\frac{\partial \mathbf{v}_0}{\partial N}\right|_N - \left.\frac{\partial \mathbf{v}_0}{\partial N}\right|_{N-1} \\ &= \mathbf{v}_{0,N} - 2\mathbf{v}_{0,N-1} + \mathbf{v}_{0,N-2}. \end{aligned} \tag{33}$$

The algorithm of the explicit time integration is summarized in Algo. 1:

Algorithm 1: Explicit cycle time integration.

1: Simulate $N \geq 3$ cycles
2: Cycle jump with Eq. (31) $\rightarrow \mathbf{v}_{0,N+\Delta N}$
3: Return

3.2. Implicit cycle scale time integration

The explicit extrapolation is solely based on past results. In the implicit scheme the values after the cycle jump are also considered ($\mathbf{v}_{0,N+\Delta N}$ and $\mathbf{v}_{q,N+\Delta N}$), as displayed in Fig. 3. Index 0 indicates the start of a load cycle and index q the end. Values at time steps in between are denoted by index l.

Following [44] we use a trapezoidal integration rule to extrapolate the variables:

$$\mathbf{v}_{0,N+\Delta N} = \mathbf{v}_{0,N} + \frac{\Delta N}{2}\left(\left.\frac{\partial \mathbf{v}_0}{\partial N}\right|_{N+\Delta N} + \left.\frac{\partial \mathbf{v}_0}{\partial N}\right|_N \right), \tag{34}$$
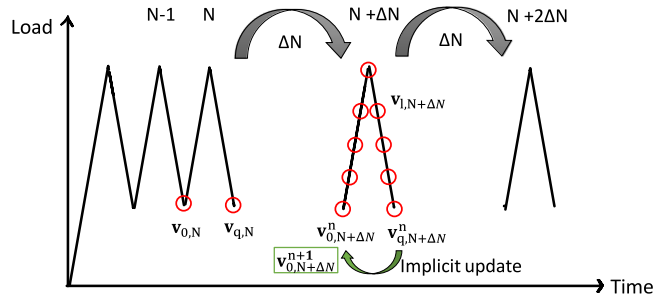
Fig. 3. Implicit cycle jump scheme.

with

$$\left. \frac{\partial \mathbf{v}_0}{\partial N} \right|_{N+\Delta N} = \mathbf{v}_{q,N+\Delta N} - \mathbf{v}_{0,N+\Delta N} \tag{35}$$

and

$$\left. \frac{\partial \mathbf{v}_0}{\partial N} \right|_{N} = \mathbf{v}_{q,N} - \mathbf{v}_{0,N}. \tag{36}$$

$\mathbf{v}_{q,N+\Delta N}$ and $\mathbf{v}_{0,N+\Delta N}$ are initially unknown. Therefore, we use a first order Taylor series to approximate:

$$\mathbf{v}_{0,N+\Delta N}^{n} = \mathbf{v}_{0,N} + \Delta N \left. \frac{\partial \mathbf{v}_0}{\partial N} \right|_{N}. \tag{37}$$

Exponent n denotes the iteration of the implicit scheme (see Fig. 3). A full load cycle is then calculated so that $\mathbf{v}_{q,N+\Delta N}^{n}$ is also known. Eq. (34) leads to a non-linear equation:

$$\mathbf{f}^{imp} = \left(1 + \frac{\Delta N}{2} \right) \mathbf{v}_{0,N+\Delta N} - \left(1 - \frac{\Delta N}{2} \right) \mathbf{v}_{0,N}$$
$$- \frac{\Delta N}{2} \left(\mathbf{v}_{q,N+\Delta N} + \mathbf{v}_{q,N} \right) \qquad = \mathbf{0}, \tag{38}$$

which we solve iteratively with the Newton–Raphson method:

$$\mathbf{v}_{0,N+\Delta N}^{n+1} = \mathbf{v}_{0,N+\Delta N}^{n} + \Delta \mathbf{v}_{0,N+\Delta N}^{n}, \tag{39}$$

$$\mathbf{f}^{imp} + \left(\left. \frac{\partial \mathbf{f}^{imp}}{\partial \mathbf{v}_0} \right|_{N+\Delta N} \right) \Delta \mathbf{v}_{0,N+\Delta N}^{n} = \mathbf{0}. \tag{40}$$

Inserting Eq. (40) in Eq. (39):

$$\mathbf{v}_{0,N+\Delta N}^{n+1} = \mathbf{v}_{0,N+\Delta N}^{n} - \left(\left. \frac{\partial \mathbf{f}^{imp}}{\partial \mathbf{v}_0} \right|_{N+\Delta N} \right)^{-1} \mathbf{f}^{imp}. \tag{41}$$

The tangent matrix is:

$$\left. \frac{\partial \mathbf{f}^{imp}}{\partial \mathbf{v}_0} \right|_{N+\Delta N} = \left(1 + \frac{\Delta N}{2} \right) \mathbf{I} - \frac{\Delta N}{2} \left. \frac{\partial \mathbf{v}_q}{\partial \mathbf{v}_0} \right|_{N+\Delta N}. \tag{42}$$

The calculation of $\partial \mathbf{v}_q / \partial \mathbf{v}_0 |_{N+\Delta N}$ is discussed in more detail in Section 3.2.1.

Summarizing (see also Algo. 2), the implicit scheme starts with an explicit jump to estimate variables $\mathbf{v}_{0,N+\Delta N}^{n}$. A full load cycle is then simulated to obtain $\mathbf{v}_{q,N+\Delta N}^{n}$ and $\partial \mathbf{v}_q^n / \partial \mathbf{v}_0 |_{N+\Delta N}$. By application of Eq. (41), the initial estimation of the variables is updated $\mathbf{v}_{0,N+\Delta N}^{n+1}$. This process is repeated until the residual:

$$Res = \frac{\mathbf{f}^{imp} \cdot \mathbf{f}^{imp}}{length(\mathbf{f}^{imp})}, \tag{43}$$

is smaller than $Res < Res_{target}$.

Algorithm 2: Implicit cycle time integration.

1: Simulate $N \geq 1$ cycles
2: Cycle jump with Eq. (37) $\rightarrow \mathbf{v}_{0,N+\Delta N}^n$
3: $Res = 10^5$, Res_{target}
4: **while** $Res > Res_{target}$ or $n < 2$ **do**
5:     Simulate full cycle at $N + \Delta N \rightarrow \mathbf{v}_{q,N+\Delta N}^n$, $\partial \mathbf{v}_q^n / \partial \mathbf{v}_0|_{N+\Delta N}$
6:     Eq. (41) $\rightarrow \mathbf{v}_0\Big|_{N+\Delta N}^{n+1}$
7:     $n = n + 1$
8:     $Res = \dfrac{\mathbf{f}^{imp} \cdot \mathbf{f}^{imp}}{length(\mathbf{f}^{imp})}$
9: Return

3.2.1. Tangent matrix $\partial \mathbf{v}_q / \partial \mathbf{v}_0|_{N+\Delta N}$

In this subsection the calculation of derivative $\partial \mathbf{v}_q / \partial \mathbf{v}_0|_{N+\Delta N}$ is presented. For displacement field $\mathbf{u}$ and damage field d, we follow [44] and apply the chain rule:

$$\frac{\partial \mathbf{v}_q}{\partial \mathbf{v}_0}\Big|_{N+\Delta N} = \prod_{m=0}^{q-1} \frac{\partial \mathbf{v}_{q-m}}{\partial \mathbf{v}_{q-m-1}}\Big|_{N+\Delta N}. \tag{44}$$

The change from one time step to another is:

$$\frac{\partial \mathbf{v}_l}{\partial \mathbf{v}_{l-1}}\Big|_{N+\Delta N} = \left(\frac{\partial \mathbf{f}}{\partial \mathbf{v}_l}\right)^{-1} \left(\frac{\partial \mathbf{f}}{\partial \mathbf{v}_{l-1}}\right)\Big|_{N+\Delta N}, \tag{45}$$

where $\mathbf{f}$ is a specific evolution equation for the variable $\mathbf{v}$.

The displacement field is described with $\mathbf{f}^u$, the discretization of the weak form of Eq. (25), see [20]:

$$\mathbf{f}^u = \int_{\Omega_0} g_d \left(\nabla_0 \mathbf{N}\right)^T \mathbf{P} dV - \int_{\Omega_0} \mathbf{N}^T \mathbf{b}_0 dV = \mathbf{0}, \tag{46}$$

where $\mathbf{N}$ denotes the standard shape functions and $\mathbf{P}$ the first Piola–Kirchhoff stress, see Eq. (8). The derivatives are calculated as:

$$\frac{\partial \mathbf{f}^u}{\partial \mathbf{u}_l} = \mathbf{K}_l^{uu}, \tag{47}$$

and

$$\frac{\partial \mathbf{f}^u}{\partial \mathbf{u}_{l-1}} = \mathbf{0}. \tag{48}$$

Inserting Eqs. (47) and (48) into Eqs. (44) and (45), we write:

$$\frac{\partial \mathbf{v}_q}{\partial \mathbf{v}_0}\Big|_{N+\Delta N}^{\mathbf{u}} = \mathbf{0}. \tag{49}$$

Next, we focus on damage d. The discretization of the weak form of Eq. (26) leads to:

$$\mathbf{f}^d = \int_{\Omega_0} \frac{2l_0^2}{\pi} \left(\nabla_0 \mathbf{N}\right)^T \left(\nabla_0 d\right) dV$$
$$+ \int_{\Omega_0} \mathbf{N}\left[\frac{\partial g_d}{\partial d}\left(\psi^{elas} + \zeta_d h^{\zeta_e}\right)\frac{l_0}{G_c} + \frac{1}{\pi}(2-2d)\right] dV, \tag{50}$$

$$\frac{\partial \mathbf{f}^d}{\partial \mathbf{d}_l} = \mathbf{K}_l^{dd}, \tag{51}$$

Table 1
Material parameters for the hyperelastic model.

C_1 [N/mm^2]	C_2 [N/mm^2]	C_3 [N/mm^2]
0.8766	0.0705	$1.0763 \cdot 10^{-06}$

Table 2
Phase-field fracture parameters.

G_c [N/mm]	l_0 [mm]	a [-]
6.0	0.25	1.88

and

$$\frac{\partial \mathbf{f}^d}{\partial \mathbf{d}_{l-1}} = \mathbf{0}. \tag{52}$$

Combining Eq. (51) and (52) with Eq. (44) and (45) results in:

$$\left.\frac{\partial \mathbf{v}_q}{\partial \mathbf{v}_0}\right|_{N+\Delta N}^{d} = \mathbf{0}. \tag{53}$$

The calculation for the load history h is easier since we can directly write:

$$h_q = h_0 + s_l s_c \int \dot{\psi}^{elas} dt, \tag{54}$$

and calculate the derivative:

$$\left.\frac{\partial \mathbf{v}_q}{\partial \mathbf{v}_0}\right|_{N+\Delta N}^{h} = \mathbf{I}. \tag{55}$$

3.2.2. Adaptive time stepping

An adaptive cycle jump procedure for the implicit scheme is proposed in this subsection. Depending on the non-linearity of the structural response, the jump size is adapted. We simply measure the non-linearity with the number of iterations of the implicit scheme, i.e. n.

The number of iterations, n, is then compared to n_{max}. We distinguish between three cases:

- $n = n_{max}$: The implicit scheme did not converge at all. The jump is repeated with a reduced jump size.
- $n = 2$: The implicit scheme converged fast. The next jump size is increased by factor N_{scale}.
- $\frac{n_{max}}{2} \leq n < n_{max}$: The implicit scheme converged slowly. The next jump size is decreased.

The jump size is at least 3 and maximally ΔN_{max}. We initialize $\Delta N_{max} = \infty$, but reduce it to $N_{max} = \Delta N$ if the scheme did not converge and the jump must be repeated. If the rate of damage before and after the jump is constant, the factor is $N_{scale} = 3$, but it decreases with increasing damage:

$$N_{scale} = 3 / \left(1 + \frac{\sum_j^{nodes}(d_{q,N+\Delta N} - d_{0,N+\Delta N})_j}{1 + \sum_j^{nodes}(d_{q,N} - d_{0,N})_j}\right). \tag{56}$$

The algorithm is summarized in Algo.3.

4. Examples: Explicit and implicit cycle jumps

In this section, we apply the explicit and implicit cycle jump schemes to three different examples and evaluate the speed up. The first simulations use a fixed step size, so that the adaptive method can be evaluated based on the results. For all simulations in this section, we use the material parameters presented in Tables 1–3.[8]

---

[8] The presented material parameters are identical to the parameters identified in [1].

Algorithm 3: Adaptive implicit cycle time integration.

1: Simulate $N \geq 1$ cycles
2: Cycle jump ΔN with Eq. (37) $\rightarrow \mathbf{v}_{0,N+\Delta N}^n$
3: $Res = 10^5$, Res_{target}, n_{max}
4: **while** $\left(Res > Res_{target} \text{ or } n < 2\right)$ and $n < n_{max}$ **do**
5:     Simulate full cycle at $N + \Delta N \rightarrow \mathbf{v}_{q,N+\Delta N}^n$, $\left. \partial \mathbf{v}_q^n / \partial \mathbf{v}_0 \right|_{N+\Delta N}$
6:     Eq. (41) $\rightarrow \left. \mathbf{v}_0 \right|_{N+\Delta N}^{n+1}$
7:     $n = n + 1$
8:     $Res = \frac{\mathbf{f}^{imp} \cdot \mathbf{f}^{imp}}{length(\mathbf{f}^{imp})}$
9: **if** $n = n_{max}$ **then**
10:     $\Delta N_{max} = \Delta N$
11:     $\Delta N = 3$
12:     Reset and return to line 2
13: **else if** $n = 2$ **then**
14:     Eq. (56) $\rightarrow N_{scale}$
15:     $\Delta N = min\left(\Delta N \cdot N_{scale}, \Delta N_{max}\right)$
16: **else if** $n > \frac{n_{max}}{2}$ **then**
17:     $\Delta N = max\left(round\left(\Delta N / 2\right), 3\right)$
18: Return

Table 3
Phase-field fatigue parameters.

ζ_d [N/mm^2]	ζ_e [−]	ζ_t [N/mm^2]	ζ_p [mm^2/N]
$1.00 \cdot 10^{-06}$	3.0	0	0

4.1. Uniaxial cyclic tension

At first, we consider uniaxial cyclic tension of a slender bar (length 2.0 mm, width 0.25 mm and thickness 0.25 mm). Unloading takes place until 20% of the maximum load. We compare in the top of Fig. 4 the number of load cycles to failure for the explicit and implicit schemes with full simulations of all load cycles. Both, the implicit and explicit schemes, use a constant jump $\Delta N = 15$. The error from the accelerated calculation is small, but the calculation time (see bottom of Fig. 4) is greatly reduced. Comparing the results for the implicit and explicit scheme, we see that the former is slightly faster. The implicit scheme is faster, since after the jump only one complete cycle has to be simulated, while the explicit scheme requires three cycles for the second-order Taylor expansion (see Eq. (31)). Therefore, we also apply an explicit scheme with a first order Taylor series extrapolation (green dotted line in Fig. 4):

$$\mathbf{v}_{0,N+\Delta N} = \mathbf{v}_{0,N} + \Delta N \left. \frac{\partial \mathbf{v}_0}{\partial N} \right|_N. \tag{57}$$

This scheme also requires the simulation of only one complete cycle after the jump, making it faster than the implicit scheme. But since it is unable to produce converging solutions for more than $N > 200$ load cycles, it is not further used.

Critical for the final calculation time is the selected jump ΔN. If ΔN is too small, the calculation time will not reduce substantially. However, the simulation may not converge if a too large value is used. We see in Fig. 4 that the error for the constant jump $\Delta N = 15$ decreases with the number of load cycles, whereas the time savings relative to the full simulation remains the same.

A study of the influence of jump size ΔN is presented in Fig. 5. The applied stretch ratio is $\lambda = 1.25$. Increasing the jump size, the error increases but calculation time is reduced. No convergence issues are encountered with
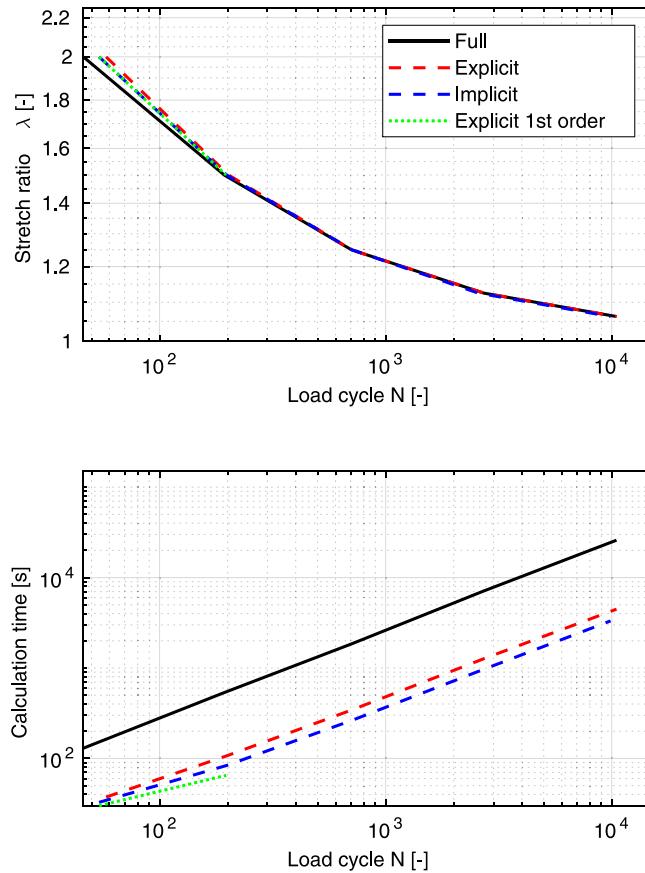
Fig. 4. Uniaxial cyclic tension: Stretch ratio versus load cycles to failure (top) and calculation time versus load cycles (bottom). The jump size is fixed to $\Delta N = 15$.

the explicit scheme, even with a large jump size of $N = 300$. This is mainly due to the simplicity of the uniaxial test case, as we cannot confirm this for the more complex case in Section 4.2. In our opinion, a good compromise between accuracy and speed up is a jump size $\Delta N = 75 \approx 10\% N_{max, full}$.

We set, therefore, for the next study the jump to ten percent of the number of load cycles to failure of the full simulations ($\Delta N = 10\% N_{max, full}$). The results for this jump step size are presented in Fig. 6. While the error is still small, the relative speed up increases. For a stretch ratio $\lambda = 1.0625$ the relative error of the results of the full calculation and the implicit scheme is 3.0%, while the implicit scheme is 200 times faster than the full calculation. However, the number of load cycles to failure is normally not known beforehand and we recommend the use of an adaptive cycle jump procedure (see Section 4.1.1).

4.1.1. Uniaxial cyclic tension: Adaptive time stepping

The performance of the adaptive cycle jump procedure for the implicit scheme is examined in this subsection. We set the initial jump $\Delta N = 5$, $\Delta N_{max} = \infty$ and $n_{max} = 6$. The results for uniaxial cyclic tension are presented in Fig. 7. All schemes show nearly the same number of load cycles to failure and the calculation time is reduced compared to the implicit scheme with $\Delta N = 15$. It is not as fast as the implicit scheme with $\Delta N = 10\% N_{max, full}$, but it does not require $N_{max, full}$ to be known beforehand.

4.2. Single edge notched tensile fatigue test

The next example considers a specimen with an initial crack. We present in Fig. 8 the dimensions, boundary conditions and the fatigue crack growth for stretch ratio $\lambda = 1.5$.
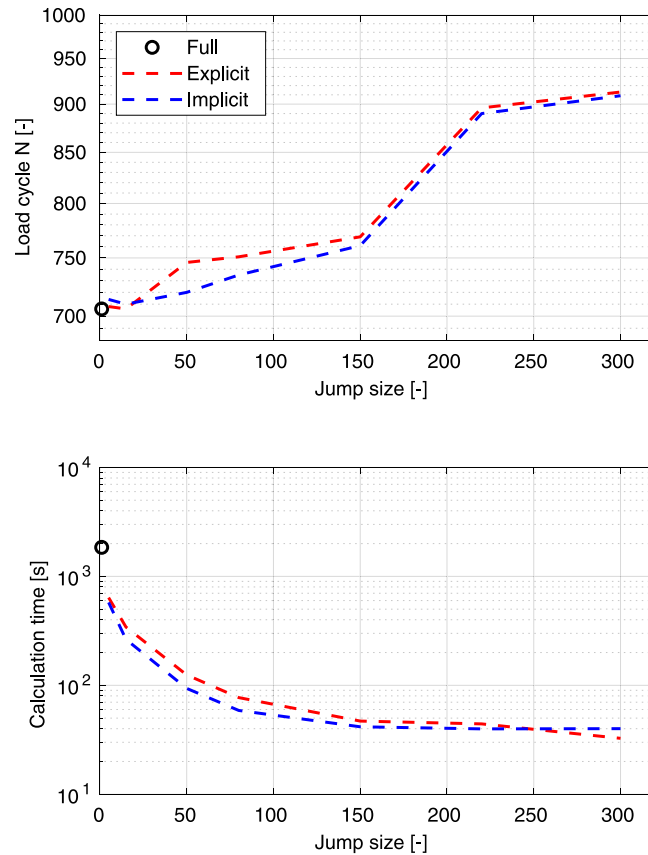
Fig. 5. Uniaxial cyclic tension: Load cycles to failure versus jump size (top) and calculation time versus jump size (bottom). The stretch ratio is fixed to $\lambda = 1.25$.

Calculating the load cycles to failure depending on the stretch ratio λ, the results for the full, explicit, implicit and adaptive schemes are presented in Fig. 9. The jump size is $\Delta N = 10$ for all simulations, except for $\lambda = 1.5$. Here, the explicit scheme only converges with $\Delta N = 2$ and the implicit scheme with $\Delta N = 5$. The larger the stretch ratio, the faster history variable grows, as well as the damage variable. This adds more nonlinearity to the system and requires a smaller jump size. The adaptive scheme always starts with $\Delta N = 5$.

All schemes reduce the calculation time, while the lifetime is not significantly affected. The implicit scheme is faster than the explicit scheme, while the main advantage of the adaptive scheme is a calculation time which weakly correlates with the number of load cycles to failure.

Interestingly, the calculation time for the adaptive scheme does not increase for an increase in the number of load cycles. A large number of load cycles corresponds to smaller applied stretch (Fig. 9) and hence, the nonlinearity is reduced. This results in turn in large jump sizes and fast calculations. Similar observations are made for the next example (Fig. 13).

A study of the influence of jump size ΔN is presented in Fig. 10. For all cases, the stretch ratio is $\lambda = 1.25$. An increase of the jump size leads to a larger error while the calculation time is reduced. The maximum jump size for the explicit scheme is $\Delta N = 15$ and for the implicit $\Delta N = 20$. In the previous section, we have concluded that a good compromise between accuracy and speed up is achieved with jump size $\Delta N = 10\% N_{max,full}$. This jump size would be too large for the current case and highlights that the selection should not only depend on the load level (Figs. 5 and 10 both present results for $\lambda = 1.25$), but also on the test case.

Additionally, we compare in Fig. 11 the final crack path for the full, direct numerical simulations and all acceleration schemes. Due to the different jump sizes and load cycles to failure, the plots are at different discrete load cycles. For stretch ratio $\lambda = 1.125 - 1.5$, only a small deviation between the results of the different schemes and the direct numerical simulation can be observed.
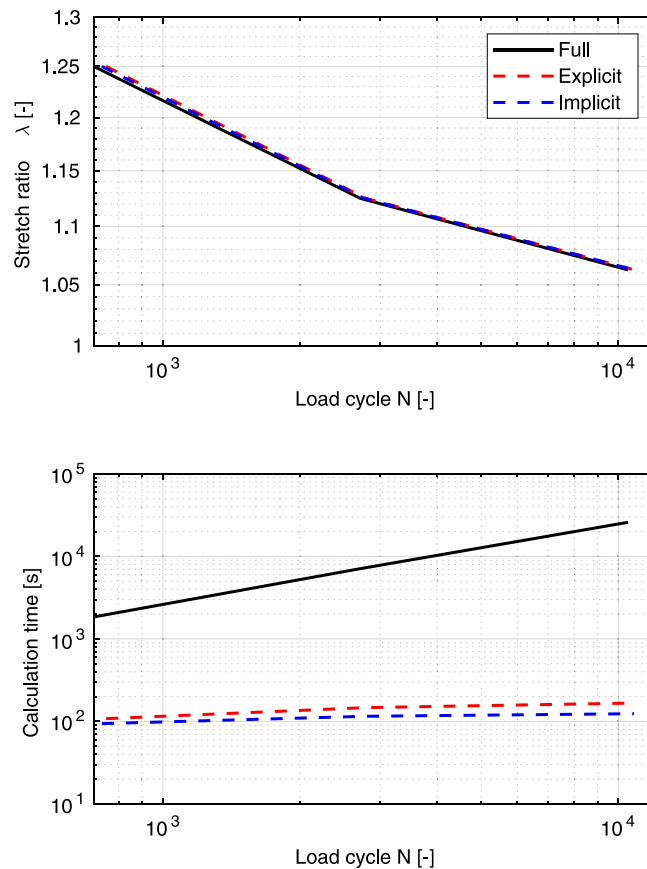
Fig. 6. Uniaxial cyclic tension: Stretch ratio versus load cycles to failure (top) and calculation time versus load cycles (bottom). The jump size is fixed to $\Delta N = 10\% N_{max,full}$.

4.3. Bending beam test

The next example considers a more complex geometry and includes regions with tensile and compressive stresses. The geometry and boundary conditions are presented in Fig. 12. We calculate the load cycles to failure depending on the displacement boundary condition for the full cycle by cycle simulation and the implicit scheme with adaptive cycle jump size.

For a prescribed displacement $u_b = 12$ mm at the right end of the beam, the crack nucleates after 295 load cycles and the part fails after 315 cycles (see Fig. 12). The crack initiates at the top, the region of the maximum tensile stress. While the implicit scheme shows a calculation time, which does not correlate the number of load cycles, the computing time for the full cycle by cycle simulation increases significantly (see Fig. 13). A full cycle by cycle calculation is computationally too costly for $u_b \leq 6$ mm.

In Fig. 14, we compare the final crack geometries predicted by the direct numerical simulations and the adaptive implicit scheme for a prescribed displacement $u_b = 6 - 12$ mm. Again, for all loads, only a small deviation can be observed.

In summary, we can state that both the explicit and implicit schemes reduce the calculation time. The implicit scheme is slightly faster than the explicit scheme that is based on second-order Taylor series. Explicit procedures based on first-order Taylor series are not recommended as convergence is not always guaranteed. Not only the reduction of the computation time, but also the accuracy of the results compared to those of the direct numerical simulation mainly depend on the selected jump size.

On the one hand, if the jump size is too small, the speed up is only marginal. On the other hand, if the jump size is too large, the simulation might not converge. To select an appropriate jump size, not only the specific case,
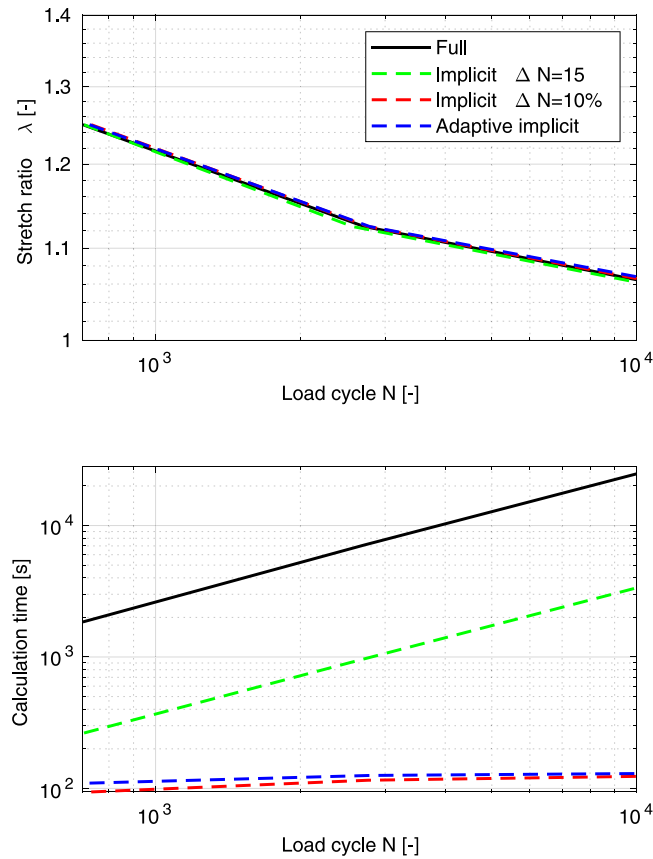
Fig. 7. Uniaxial cyclic tension: Stretch ratio versus load cycles to failure (top) and calculation time versus load cycles (bottom).
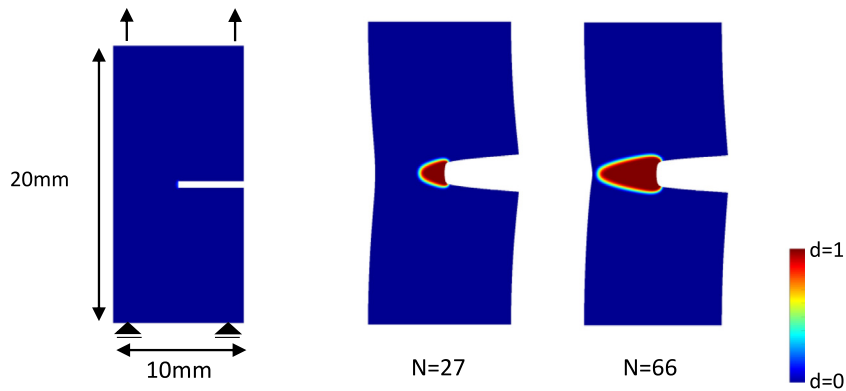

Fig. 8. Single edge notched tensile fatigue test: Dimensions of the sample, boundary condition and fatigue crack growth for stretch ratio $\lambda = 1.5$ predicted by the direct numerical simulation.

but also the expected lifetime must be considered. Slightly larger jump sizes can be used for the implicit scheme than for the explicit scheme.

The presented adaptive scheme automatically adjusts the jump size depending on the required number of iterations. As a result, computing times that are almost independent of the number of load cycles are achieved. Hence, we use the adaptive implicit scheme in the remainder of this study.
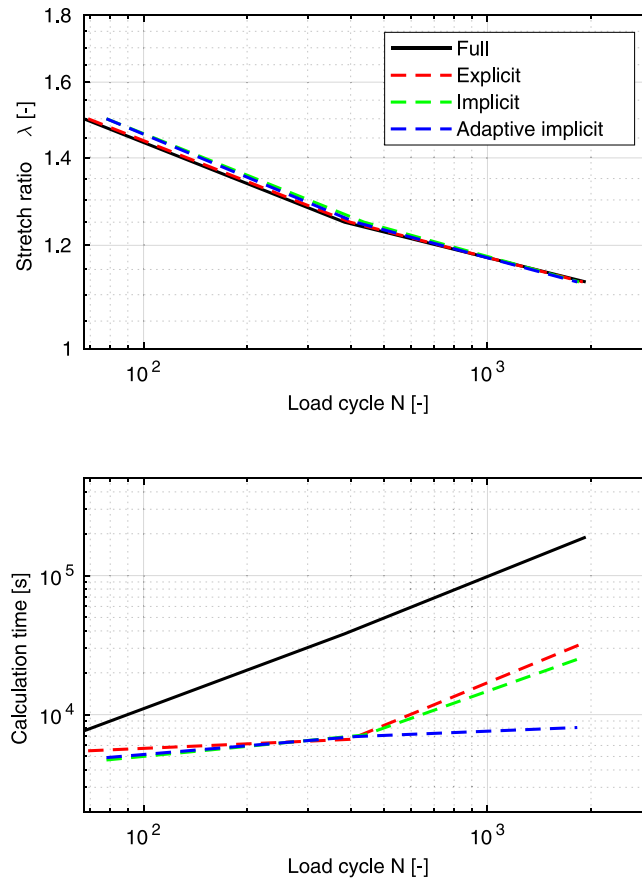
Fig. 9. Single edge notched tensile fatigue test: Stretch ratio versus load cycles to failure (top) and calculation time versus load cycles (bottom).

Table 4
Identified hyperelastic material parameters.

C_1 [N/mm^2]	C_2 [N/mm^2]	C_3 [N/mm^2]
0.2807	0.01045	$1.0213 \cdot 10^{-06}$

5. Results: Experimental validation

We experimentally validate the model in this section. First, we explain the material parameter identification, followed by experimental and numerical results for fatigue crack nucleation and crack propagation. Plane stress conditions occur in all experiments and are also incorporated in all simulations.

5.1. Material parameters

An EPDM rubber is used for all experiments at a constant temperature of $20°C$. Since the focus of this work is on fatigue failure, the hyperelastic material parameters are fitted to the reloaded uniaxial response between stretch ratio $\lambda = 1.5 - 2.9$. Note that the initial material response is much stiffer. The parameters are presented in Table 4 and the fit in Fig. 15.

The phase-field fracture parameters are shown in Table 5. Parameters $l_0 = 0.25$ and $a = 1.88$ are taken from our previous work [1], while fracture toughness $G_c = 2.25 N/mm$ is adapted to the results for monotonic loading (see load cycle $N = 1$ in Figs. 16 and 20). The adjustment of G_c is necessary since we neglect rate-dependent effects
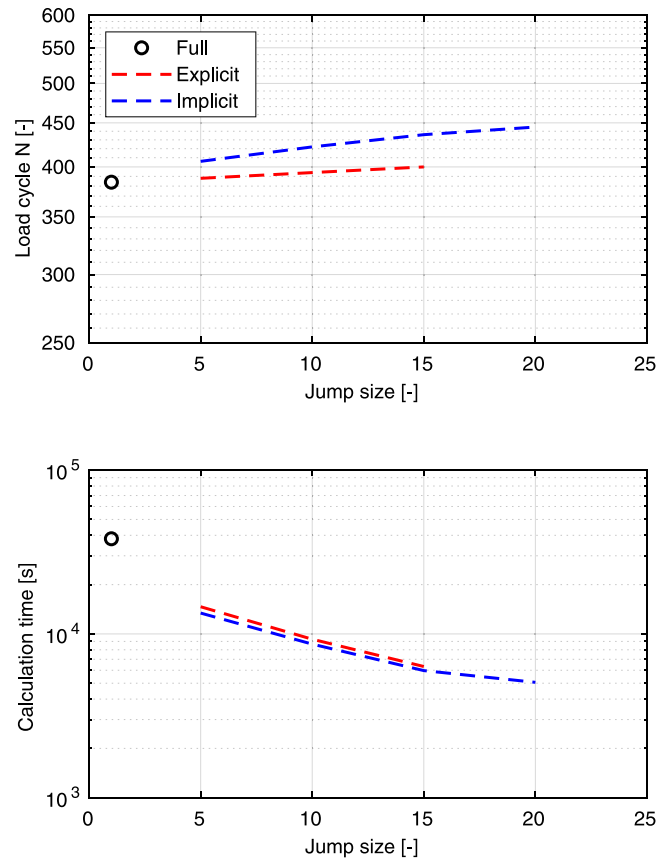
Fig. 10. Single edge notched tensile fatigue test: Load cycles to failure versus jump size (top) and calculation time versus jump size (bottom). The stretch ratio is fixed to $\lambda = 1.25$.

Table 5
Identified phase-field fracture material parameters.

G_c [N/mm]	l_0 [mm]	a [$-$]
2.25	0.25	1.88

Table 6
Identified phase-field fatigue material parameters.

ζ_d [N/mm^2]	ζ_e [$-$]	ζ_t [N/mm^2]	ζ_p [mm^2/N]
$4.01 \cdot 10^{-06}$	1.9	1.6	25

in this work (see Table 4). We want to point out that $l_0 = 0.25$ mm was fitted to local strain measurements close to crack tip [1].

The fatigue material parameters (Table 6) are identified by minimizing a least-squares objective function with the experimental load cycles to failure of uniaxial tensile tests (Section 5.2) and single edge notched tensile fatigue test (Section 5.3) with a genetic algorithm. Hence, the results of pure-shear crack growth in Section 5.4 are true predictions without further calibration of the parameters.

5.2. Uniaxial tensile test

A dumbbell specimen according to ISO 37 is subjected to a cyclic load. We measure the number of load cycles to failure depending on the applied maximum stretch. The minimum stretch ratio for all load levels is
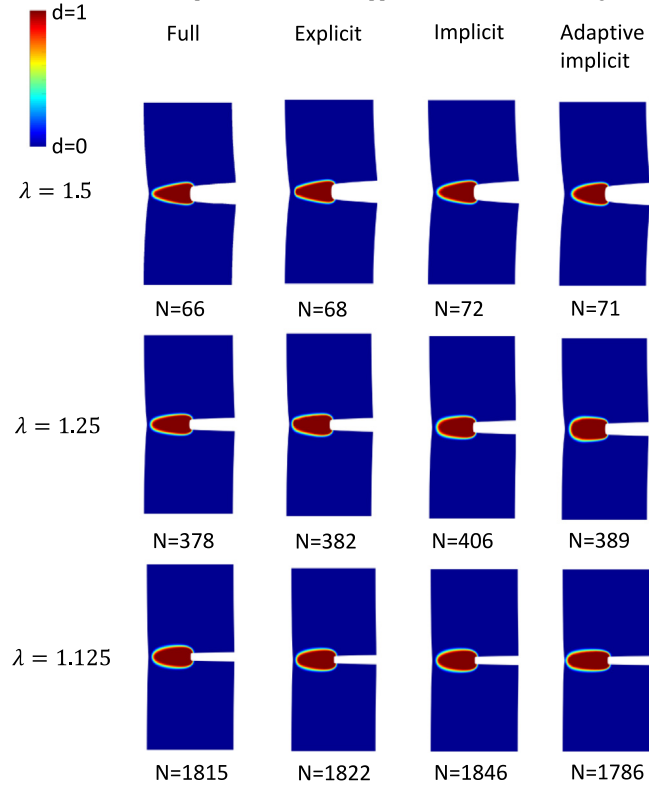
Fig. 11. Single edge notched tensile fatigue test: Final crack paths for stretch ratio $\lambda = 1.125 - 1.5$.
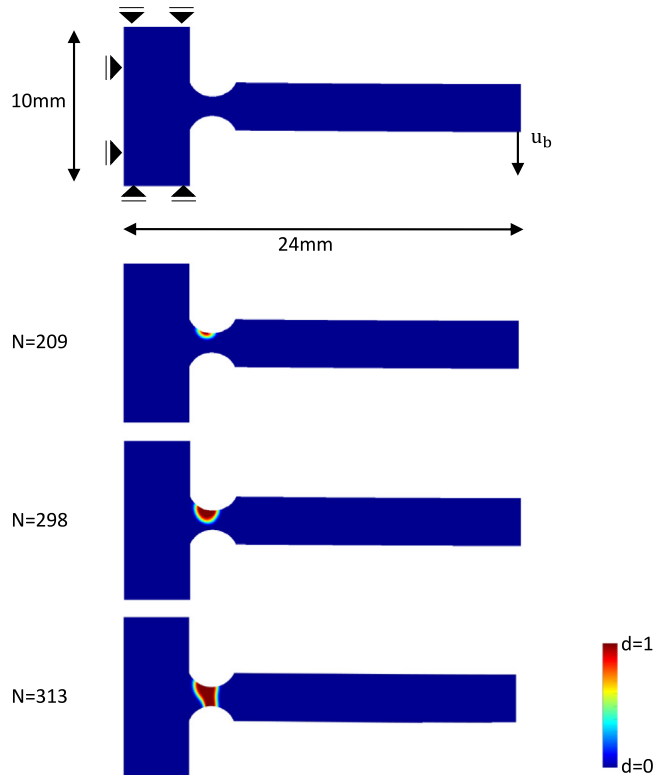
Fig. 12. Bending beam test: Dimensions of the sample, boundary condition and fatigue crack growth for displacement $u_b = 12$ mm predicted by the adaptive scheme.
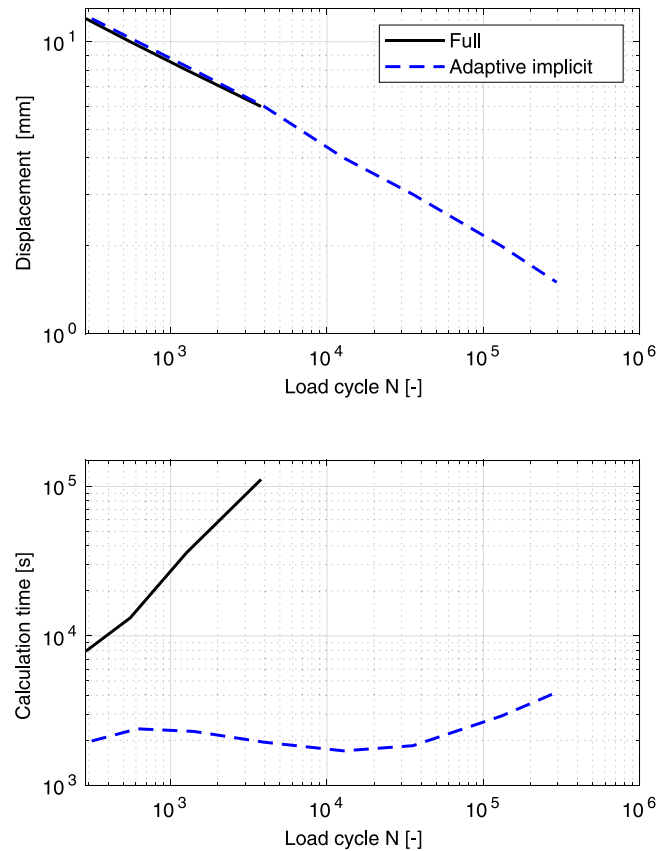
Fig. 13. Bending beam test: Displacement versus load cycles to failure (top) and calculation time versus load cycles (bottom).

$\lambda_{min} = 1.5$. Fig. 16 shows the experimental and numerical results. The prediction of the lifetime agrees well with the experimental median value.

We note that, the experimental results show a wide scattering. A reason for this could be the random dispersion of large agglomerates. It is known, see e.g. [58] or [71], that fatigue failure of rubber is dependent on the size and distribution of initial flaws. Samples with early failure were characterized with one or more large flaws on the fracture surface. Cracks originate at this location and grow until final rupture (see Fig. 17).

5.3. Single edge notched tensile fatigue test

Next, we investigate fatigue crack growth for specimens according to ISO 34.[9] The dimensions, boundary conditions and the numerically predicted crack growth for monotonic loading are presented in Fig. 18. In Fig. 19, an experimental ruptured sample is documented. The numerically predicted crack path is identical to its experimental counterpart. Furthermore, we compare the numerically predicted and experimentally measured number of load cycles to failure (Fig. 20). The prediction of our model agrees well with the experimental results.

5.4. Pure shear fatigue crack growth

Finally, we validate the model by measuring the fatigue crack growth rate in a pure shear setting according to ISO 27727. The pure shear specimen is characterized by a large width relative to its height and is presented in Fig. 21. Applying a cyclic load, the crack length can be measured as a function of the number of load cycles (Fig. 22). Two

---

[9] The experimental results are taken from [1]. We observe a poorer match between the model and the experiments, since we also consider uniaxial tensile test data in the parameter identification.
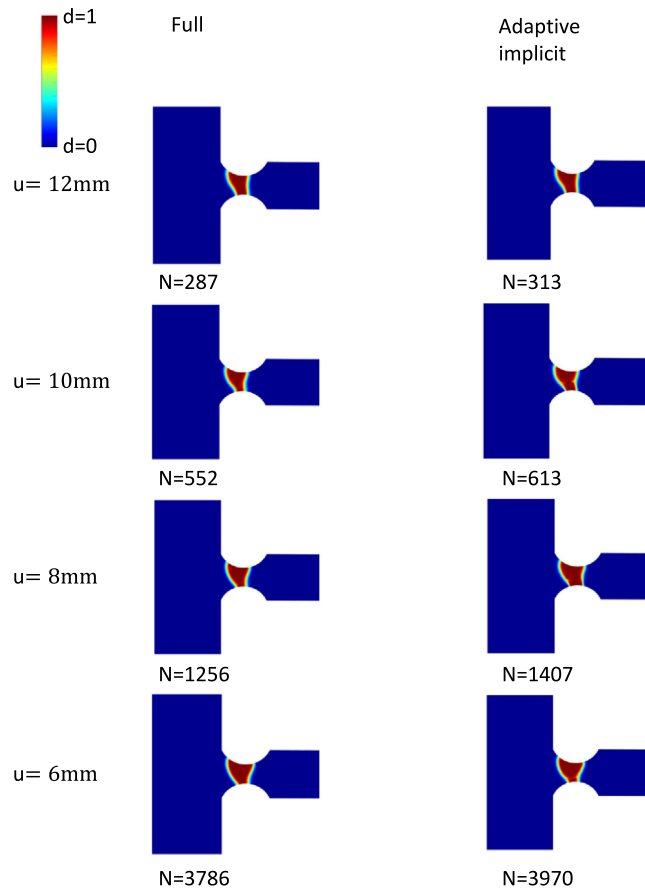
Fig. 14. Bending beam test: Fatigue cracks for displacement $u_b = 6 - 12$ mm.
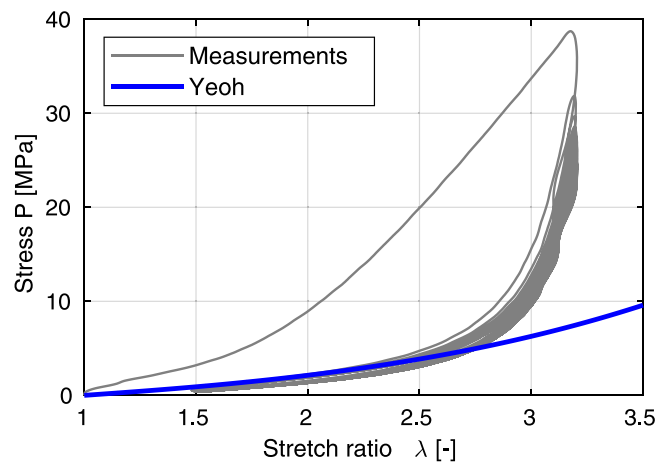

Fig. 15. Uniaxial tensile test: Stress versus stretch-ratio. We compare the material model to the experimental observation.

samples were tested and the average crack growth rate as a function of the tearing energy $G = z_o \psi^{elas}$ is presented in Fig. 23. Comparing the experimental results to the model predictions, we see a good correlation. The damage field (Fig. 21) appears large, but is the consequence from a length scale $l_0 = 0.25$ mm experimentally obtained
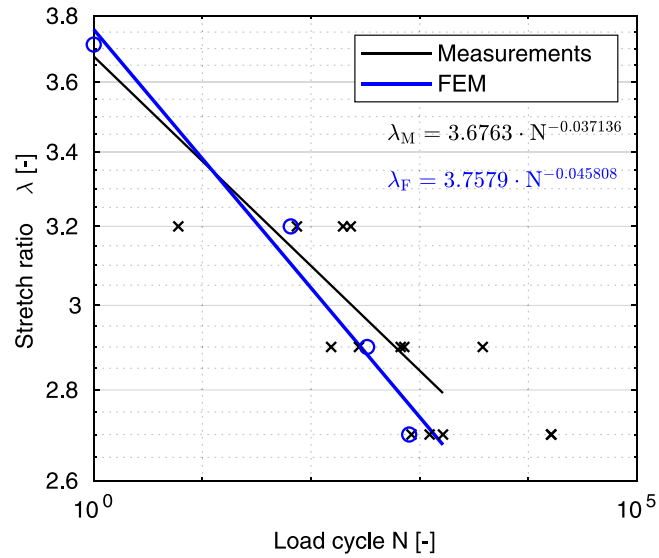
Fig. 16. Fatigue uniaxial tensile test: Stretch ratio versus load cycle to failure. The lines represent the least-squares trends of the experimental results (black crosses) and the simulations (blue circles).
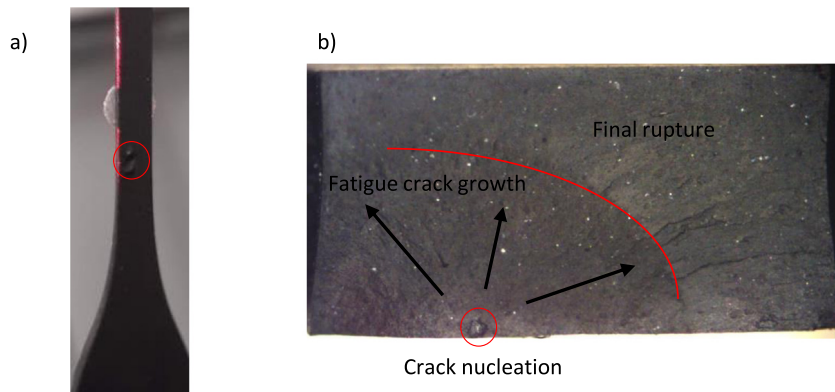
Fig. 17. Fatigue uniaxial tensile test: Crack nucleation (a) and final fracture surface (b). The crack initially formed at the largest inclusion.
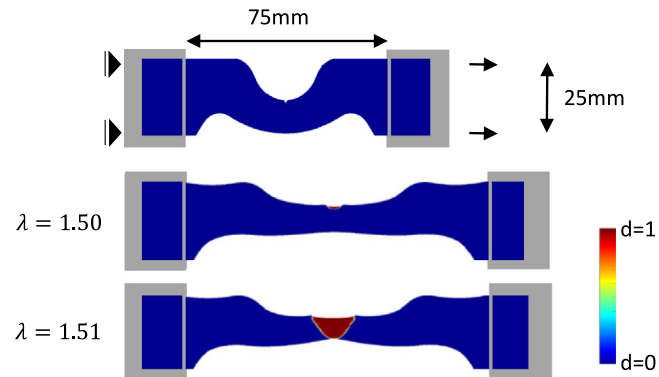

Fig. 18. SENT according to ISO34-1, type C: Specimen dimensions, boundary condition and numerically predicted damage field for monotonic loading.
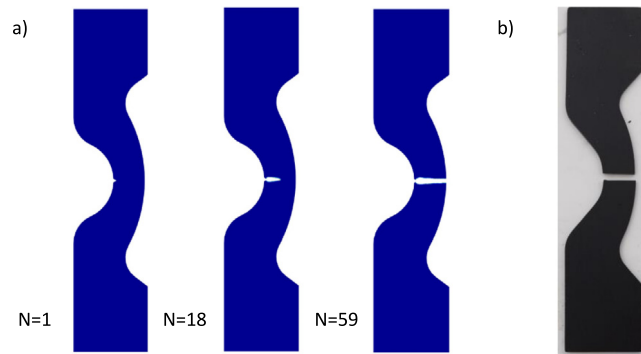
Fig. 19. SENT according to ISO34-1, type C: (a) Numerically predicted fatigue crack growth for stretch ratio $\lambda = 1.4$. Elements with $d > 0.95$ are not plotted. (b) Experimentally observed crack geometry.
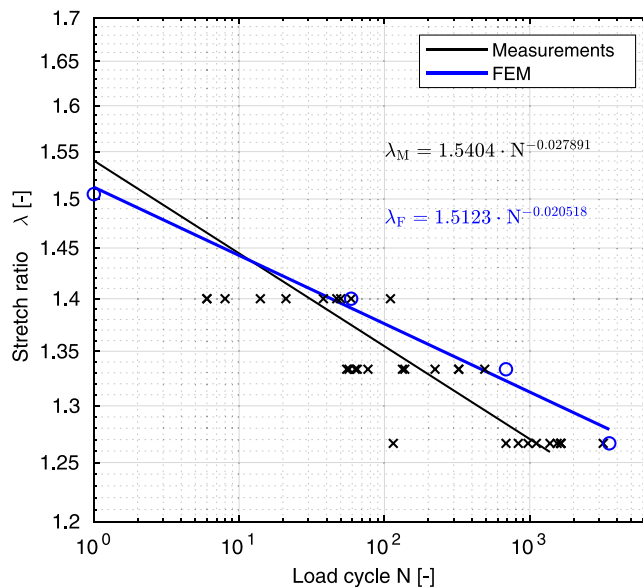

Fig. 20. Fatigue SENT according to ISO34-1, type C: Stretch ratio versus load cycle to failure. The lines represent the least-squares trends of the experimental results (black crosses) and the simulations (blue circles).

from local strain measurements and a small sample height ($z_0 = 2$ mm). The kinking of the crack in the tests also indicates a larger process zone at the crack tip (Fig. 22).

6. Concluding remarks

In the context of phase-field damage models, an extension to predict fatigue damage is achieved by introducing a fatigue damage source in the balance of mechanical energy. To accelerate fatigue simulations, explicit and implicit cycle jump schemes are presented. Both schemes reduce the calculation time significantly, while the accuracy remains largely unaffected. As the size of the cycle jump step governs the speed up of the simulations, but may also be responsible for the failure of a simulation, an adaptive cycle jump scheme for the implicit acceleration framework is proposed based on the number of iterations. The maximum acceleration achieved by the implicit scheme was 99.5%.

Thanks to extensive measurements, all material parameters are identified from experiments. The adaptive implicit scheme decreases the computation times so much that we were even able to identify the fatigue material parameters — with uniaxial fatigue tensile tests on dumbbell specimens (ISO 37) and fatigue crack growth experiments
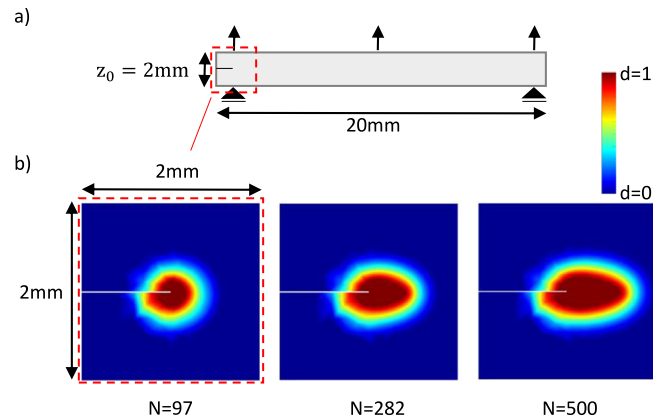
Fig. 21. Pure shear fatigue crack growth: (a) Dimensions and boundary conditions. The minimal force in a load cycle is zero. (b) Damage propagation at the crack tip.

Fig. 22. Pure shear fatigue crack growth: Experimentally observed crack geometry (from top to bottom).

according to ISO 34. While the lifetime of the dumbbell specimens is underestimated, the lifetime of specimens according to ISO 34 is slightly overestimated. We validate the model and identified material parameters with fatigue crack growth measurements according to ISO 27727.

These examples suggest that the fatigue phase-field damage model is able to describe the three stages of (fatigue) failure: crack initiation, crack propagation and final fracture. Future work will focus on a three-dimensional implementation so that the influence of multiaxial loading can more accurately be investigated. Furthermore, high-cycle fatigue experiments would experimentally validate the model for more than 10^6 load cycles.

Declaration of competing interest

The authors declare that they have no known competing financial interests or personal relationships that could have appeared to influence the work reported in this paper.
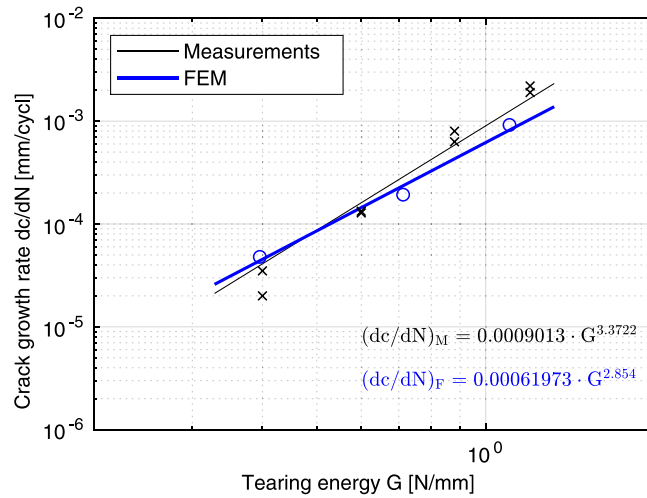
Fig. 23. Pure shear fatigue crack growth: Crack growth rate versus the tearing energy. The lines represent the least-squares trends of the experimental results (black crosses) and the simulations (blue circles).
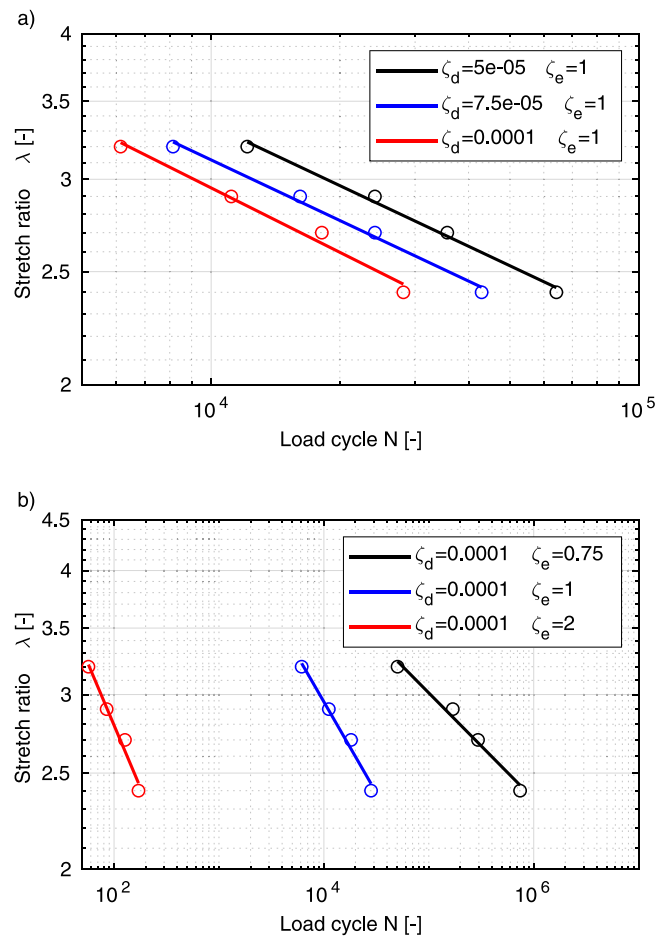

Fig. A.24. Uniaxial cyclic tension: Stretch ratio versus number of load cycles to failure for different values of multiplier ζ_d (top) and exponent ζ_e (bottom).
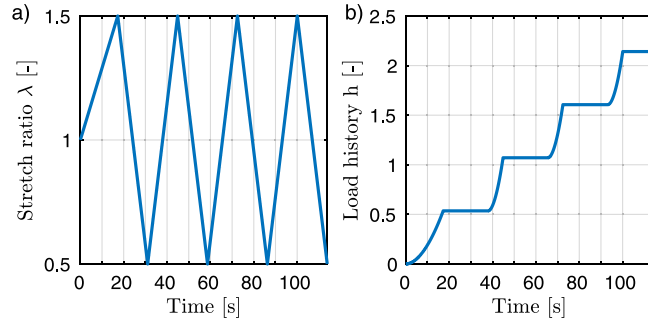
Fig. B.25. Uniaxial tension–compression: (a) Stretch-ratio versus time. (b) Load history versus time. A compressive load does not increase the load history.
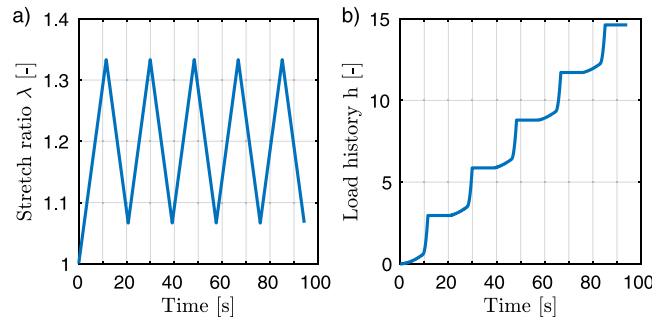

Fig. B.26. Equibiaxial tension: (a) Stretch-ratio versus time. (b) Load history versus time. The load history grows faster after reaching threshold ζ_t.
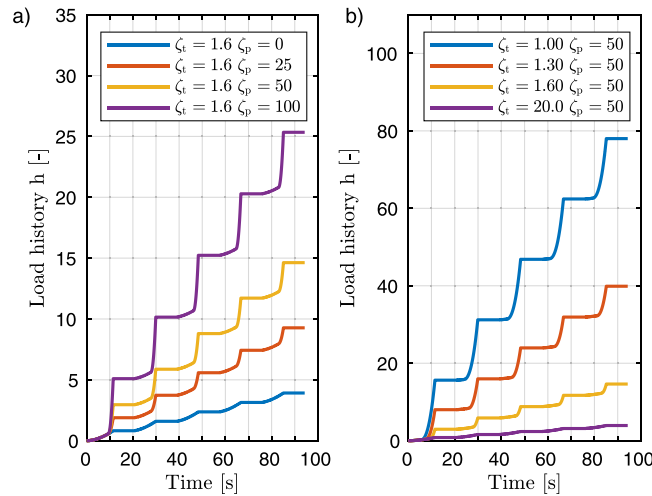

Fig. B.27. Equibiaxial tension: Load history versus time for different values of (a) ζ_p and (b) ζ_t.

Appendix A. Parametric study: Fatigue parameters ζ_d and ζ_e

Considering uniaxial cyclic tension and measuring the cycles to failure, we present in Fig. A.24 so-called Woehler lines. We use the hyperelastic and phase-field fracture material parameters from Tables 4 and 5. The fatigue phase-field parameters ζ_d and ζ_e are varied as shown in Fig. A.24 ($\zeta_p = 0$ and $\zeta_t = 0$).
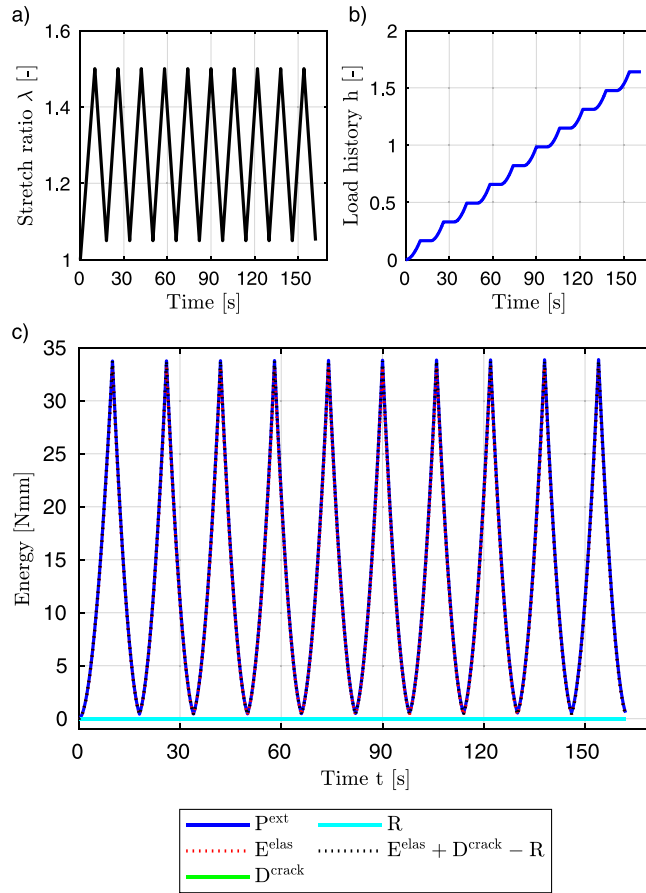
Fig. C.28. Uniaxial cyclic tension: (a) Stretch-ratio versus time. (b) Load history versus time. (c) Energy versus time for the different components of the model. The balance of mechanical energy (Eq. (1)) is satisfied for the entire time.

The multiplier (fatigue material parameter ζ_d) yields a shift of the response, whilst the exponent (fatigue material parameter ζ_e) also yields a slope difference. We conclude from the results that Eq. (22) provides a suitable framework to describe the experimental data.

Appendix B. New load history h

To demonstrate the characteristic of the new load history h we consider two test cases: Uniaxial tension–compression and equibiaxial tension. We use the material parameters presented in Section 4 (Tables 1–3) with $\zeta_t = 1.6$ and $\zeta_p = 50$. For the first case of uniaxial tension–compression (see Fig. B.25), we show that the load history does not grow for compressive stresses. Applying equibiaxial tension (Fig. B.26), we see that after reaching the threshold ζ_t the load history grows faster.

This effect is shown in more detail in Fig. B.27, by first varying ζ_p and then ζ_t. Fatigue material parameter ζ_p yields a shift of the slope, whilst fatigue material parameter ζ_t controls the start of the slope shift.

Appendix C. Balance of mechanical energy and dissipation during crack growth

We apply uniaxial cyclic tension to a bar (length 20 mm, width 10 mm and thickness 1 mm) and control the development of the energy of the various model components. The material parameters from Tables 4–6 are used.

Fig. C.28a displays the applied stretch ratio versus time and we see an increasing history variable (Fig. C.28b). No damage occurs after 10 load cycles so that $D^{crack} = R = 0$. The elastically stored energy and the applied external energy are in balance (Fig. C.28c). Therefore, we change material parameters $a = 50$ and $\beta_d = 10^3 \cdot \beta_d$
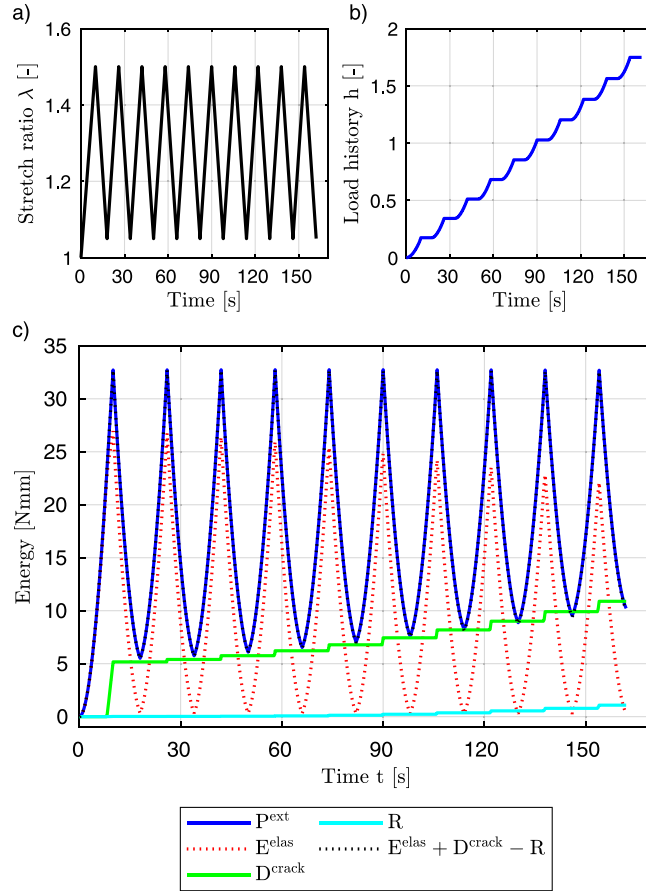
Fig. C.29. Uniaxial cyclic tension: Material parameters $a = 50$ and $\beta_d = 10^3 \cdot \beta_d$. (a) Stretch-ratio versus time. (b) Load history versus time. (c) Energy versus time for the different components of the model. The balance of mechanical energy (Eq. (1)) is satisfied for the entire time.
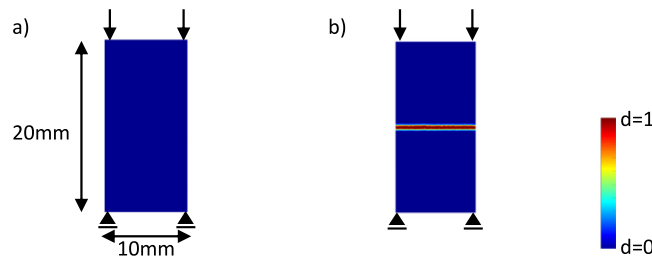

Fig. D.30. Uniaxial compression: (a) Dimensions and boundary conditions. (b) A crack is introduced by initializing the model with $d = 1$.

and present the respective results in Fig. C.29. Damage starts to grow with the first cycle, so that the elastically stored energy decreases and R increases.

Finally, we conclude from Figs. C.28 and C.29 that the model is thermodynamically consistent since the balance of mechanical energy (Eq. (1)) is fulfilled at any given time.

Appendix D. Uniaxial compression

We introduced in Eq. (28) an energy split for incompressible materials in plane stress to avoid damage growth in compression and crack surface penetration. In this appendix, the split is evaluated with two test cases. All examples
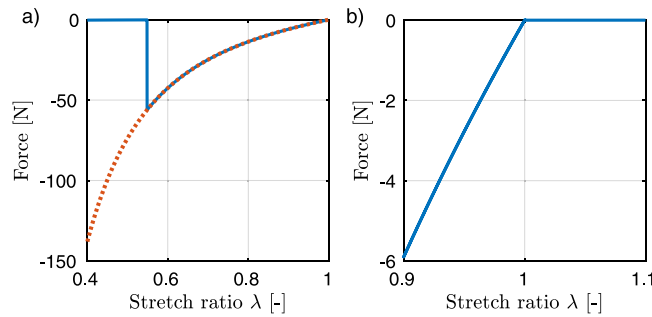
Fig. D.31. Uniaxial compression: Force versus stretch ratio: (a) Compression with the split (Eq. (28), red line) and without (blue line). (b) Compression and tension of a sample with an initial crack.

in this section use the material from Tables 1–3, except that we reduce $G_c = 0.5$ N/mm to enable faster damage growth.

First, we compress the specimen depicted in Fig. D.30a. Without the split, we observe a failure of the part (blue line, Fig. D.31) while using the split ensures that no damage occurs (red line).

The next test considers compression and tension of a sample with an initial crack (Fig. D.30b). The crack is introduced by initializing the model with $d = 1$. Using the proposed split, the sample absorbs compressive forces but is not able to transfer tensile loads (Fig. D.31b).

We conclude that the split successfully prevents both damage to grow during compression as well as crack surface penetration. Note that (resistance-free) sliding of the crack surfaces in the plane of the crack cannot be captured accurately.

References

[1] P.J. Loew, B. Peters, L.A.A. Beex, Fatigue phase-field damage modeling of rubber using viscous dissipation: Crack nucleation and propagation, Mech. Mater. 142 (2020).

[2] C. Miehe, M. Hofacker, F. Welschinger, A phase field model for rate-independent crack propagation: Robust algorithmic implementation based on operator splits, Comput. Methods Appl. Mech. Engrg. 199 (45–48) (2010) 2765–2778.

[3] C. Miehe, F. Welschinger, M. Hofacker, Thermodynamically consistent phase-field models of fracture: variational principles and multi-field FE implementations, Internat. J. Numer. Methods Engrg. 83 (10) (2010) 1273–1311.

[4] B. Bourdin, G.A. Francfort, J.J. Marigo, Numerical experiments in revisited brittle fracture, J. Mech. Phys. Solids 48 (4) (2000) 797–826.

[5] V.P. Nguyen, O. Lloberas-Valls, M. Stroeven, L.J. Sluys, Homogenization-based multiscale crack modelling: From micro-diffusive damage to macro-cracks, Comput. Methods Appl. Mech. Engrg. 200 (2011) 1220–1236.

[6] S. Wulfinghoff, A generalized cohesive zone model and a grain boundary yield criterion for gradient plasticity derived from surface- and interface-related arguments, Int. J. Plast. 92 (2017) 57–78.

[7] L.A.A. Beex, R.H.J. Peerlings, An experimental and computational study of laminated paperboard creasing and folding, Int. J. Solids Struct. 46 (24) (2009) 4192–4207.

[8] L.A.A. Beex, R.H.J. Peerlings, On the influence of delamination on laminated paperboard creasing and folding, Phil. Trans. R. Soc. A 370 (1965) (2012) 1912–1924.

[9] N. Moës, J. Dolbow, T. Belytschko, A finite element method for crack growth without remeshing, Internat. J. Numer. Methods Engrg. 46 (1) (1999) 131–150.

[10] S. Bordas, V.P. Nguyen, C. Dunant, A. Guidoum, H. Nguyen-Dang, An extended finite element library, Internat. J. Numer. Methods Engrg. 71 (6) (2007) 703–732.

[11] I.V. Singh, B.K. Mishra, S. Bhattacharya, R.U. Patil, The numerical simulation of fatigue crack growth using extended finite element method, Int. J. Fatigue 36 (1) (2012) 109–119.

[12] Y. Wang, H. Waisman, From diffuse damage to sharp cohesive cracks: A coupled XFEM framework for failure analysis of quasi-brittle materials, Comput. Methods Appl. Mech. Engrg. 299 (2016) 57–89.

[13] R.H.J. Peerlings, R. de Borst, W.A.M. Brekelmans, J.H.P. de Vree, Gradient enhanced damage for quasi-brittle materials, Internat. J. Numer. Methods Engrg. 39 (19) (1996) 3391–3403.

[14] L.H. Poh, G. Sun, Localizing gradient damage model with decreasing interactions, Internat. J. Numer. Methods Engrg. 110 (6) (2017) 503–522.

[15] G. Sun, L.H. Poh, Homogenization of intergranular fracture towards a transient gradient damage model, J. Mech. Phys. Solids 95 (2016) 374–392.

[16] C. Steinke, I. Zreid, M. Kaliske, On the relation between phase-field crack approximation and gradient damage modelling, Comput. Mech. 59 (5) (2017) 717–735.

[17] R. de Borst, C.V. Verhoosel, Gradient damage vs phase-field approaches for fracture: Similarities and differences, Comput. Methods Appl. Mech. Engrg. 312 (2016) 78–94.

[18] T.K. Mandal, V.P. Nguyen, A. Heidarpour, Phase field and gradient enhanced damage models for quasi-brittle failure: A numerical comparative study, Eng. Fract. Mech. 207 (2019) 48–67.

[19] C. Miehe, L.M. Schänzel, Phase field modeling of fracture in rubbery polymers. Part I: Finite elasticity coupled with brittle failure, J. Mech. Phys. Solids 65 (1) (2014) 93–113.

[20] P.J. Loew, B. Peters, L.A.A. Beex, Rate-dependent phase-field damage modeling of rubber and its experimental parameter identification, J. Mech. Phys. Solids 127 (2019) 266–294.

[21] J. Wu, C. McAuliffe, H. Waisman, G. Deodatis, Stochastic analysis of polymer composites rupture at large deformations modeled by a phase field method, Comput. Methods Appl. Mech. Engrg. (2016).

[22] B. San, H. Waisman, Optimization of carbon black polymer composite microstructure for rupture resistance, J. Appl. Mech. 84 (2) (2016) 021005.

[23] J.B. Russ, H. Waisman, Topology optimization for brittle fracture resistance, Comput. Methods Appl. Mech. Engrg. 347 (2019) 238–263.

[24] G. Amendola, M. Fabrizio, J.M. Golden, Thermomechanics of damage and fatigue by a phase field model, J. Therm. Stresses 39 (5) (2016) 487–499.

[25] M. Caputo, M. Fabrizio, Damage and fatigue described by a fractional derivative model, J. Comput. Phys. 293 (2015) 400–408.

[26] J.L. Boldrini, E.A. Barros de Moraes, L.R. Chiarelli, F.G. Fumes, M.L. Bittencourt, A non-isothermal thermodynamically consistent phase field framework for structural damage and fatigue, Comput. Methods Appl. Mech. Engrg. 312 (2016) 395–427.

[27] R. Alessi, S. Vidoli, L. De Lorenzis, A phenomenological approach to fatigue with a variational phase-field model: The one-dimensional case, Eng. Fract. Mech. 190 (2018) 53–73.

[28] P. Carrara, M. Ambati, R. Alessi, L. De Lorenzis, A framework to model the fatigue behavior of brittle materials based on a variational phase-field approach, Comput. Methods Appl. Mech. Engrg. 12731 (2019).

[29] A. Mesgarnejad, A. Imanian, A. Karma, Phase-field models for fatigue crack growth, Theor. Appl. Fract. Mech. 103 (2019).

[30] Y.S. Lo, M.J. Borden, K. Ravi-Chandar, C.M. Landis, A phase-field model for fatigue crack growth, J. Mech. Phys. Solids 132 (2019).

[31] T. Heister, M.F. Wheeler, T. Wick, A primal-dual active set method and predictor-corrector mesh adaptivity for computing fracture propagation using a phase-field approach, Comput. Methods Appl. Mech. Engrg. 290 (2015) 466–495.

[32] J. Cheng, X. Tu, S. Ghosh, Wavelet-enriched adaptive hierarchical FE model for coupled crystal plasticity-phase field modeling of crack propagation in polycrystalline microstructures, Comput. Methods Appl. Mech. Engrg. 361 (2019).

[33] R.U. Patil, B.K. Mishra, I.V. Singh, A local moving extended phase field method (LMXPFM) for failure analysis of brittle materials, Comput. Methods Appl. Mech. Engrg. 342 (2018) 674–709.

[34] P. Shanthraj, L. Sharma, B. Svendsen, F. Roters, D. Raabe, A phase field model for damage in elasto-viscoplastic materials, Comput. Methods Appl. Mech. Engrg. 312 (2016) 167–185.

[35] J.Y. Wu, Y. Huang, V.P. Nguyen, On the BFGS monolithic algorithm for the unified phase field damage theory, Comput. Methods Appl. Mech. Engrg. 360 (2020).

[36] W. Van Paepegem, J. Degrieck, Fatigue degradation modelling of plain woven glass/epoxy composites, Composites - Part A: Applied Science and Manufacturing 32 (10) (2001) 1433–1441.

[37] A. Turon, J. Costa, P.P. Camanho, C.G. Dávila, Simulation of delamination in composites under high-cycle fatigue, Composites A 38 (11) (2007) 2270–2282.

[38] D. Cojocaru, A.M. Karlsson, A simple numerical method of cycle jumps for cyclically loaded structures, Int. J. Fatigue 28 (12) (2006) 1677–1689.

[39] R.H.J. Peerlings, W.A.M. Brekelmans, R. De Borst, M.G.D. Geers, Gradient-enhanced damage modelling of high-cycle fatigue, Internat. J. Numer. Methods Engrg. 49 (12) (2000) 1547–1569.

[40] C. Oskay, J. Fish, Fatigue life prediction using 2-scale temporal asymptotic homogenization, Internat. J. Numer. Methods Engrg. 61 (3) (2004) 329–359.

[41] J. Heczko, R. Kottner, Modeling of material damage using finite elements and time homogenization in case of finite strain, Appl. Math. Comput. (2017) 1–10.

[42] S. Manchiraju, M. Asai, S. Ghosh, A dual-time-scale finite element model for simulating cyclic deformation of polycrystalline alloys, J. Strain Anal. Eng. Des. 42 (4) (2007) 183–200.

[43] D.S. Joseph, P. Chakraborty, S. Ghosh, Wavelet transformation based multi-time scaling method for crystal plasticity FE simulations under cyclic loading, Comput. Methods Appl. Mech. Engrg. 199 (33–36) (2010) 2177–2194.

[44] M. Beusink, Multi-Time Scale Methods for an Efficient Finite Element Analysis of Fatigue Problems (Master's thesis), Eindhoven University of Technology, 2013.

[45] M.E. Gurtin, Generalized cahn-hilliard equations based on a microforce balance, Physica 2003 (4) (1996) 178–192.

[46] M. Frémond, B. Nedjar, Damage, gradient of damage and principle of virtual power, Int. J. Solids Struct. 33 (8) (1996) 1083–1103.

[47] M.J. Borden, T.J.R. Hughes, C.M. Landis, A. Anvari, I.J. Lee, A phase-field formulation for fracture in ductile materials: Finite deformation balance law derivation, plastic degradation, and stress triaxiality effects, Comput. Methods Appl. Mech. Engrg. 312 (2016) 130–166.

[48] A. Kumar, G.A. Francfort, O. Lopez-Pamies, Fracture and healing of elastomers: A phase-transition theory and numerical implementation, J. Mech. Phys. Solids (2018).

[49] H. Stumpf, K. Hackl, Micromechanical concept for the analysis of damage evolution in thermo-viscoelastic and quasi-brittle materials, Int. J. Solids Struct. 40 (6) (2003) 1567–1584.

[50] J.Y. Wu, P.V. Nguyen, A length scale insensitive phase-field damage model for brittle fracture, J. Mech. Phys. Solids 119 (l) (2018) 20–42.

[51] J.Y. Wu, A unified phase-field theory for the mechanics of damage and quasi-brittle failure, J. Mech. Phys. Solids 103 (2017) 72–99.

[52] O.H. Yeoh, Some forms of the strain energy function for rubber, Rubber Chem. Technol. 66 (5) (2011) 754–771.

[53] R. Shen, H. Waisman, L. Guo, Fracture of viscoelastic solids modeled with a modified phase field method, Comput. Methods Appl. Mech. Engrg. 346 (2019) 862–890.

[54] D. Aranda-Iglesias, G. Vadillo, J.A. Rodríguez-Martínez, K.Y. Volokh, Modeling deformation and failure of elastomers at high strain rates, Mech. Mater. 104 (2017) 85–92.

[55] V. Le Saux, Y. Marco, S. Calloch, P. Charrier, D. Taveau, Heat build-up of rubber under cyclic loadings: Validation of an efficient demarch to predict the temperature fields, Rubber Chem. Technol. 86 (1) (2013) 38–56.

[56] Y. Lev, A. Faye, K.Y. Volokh, Thermoelastic deformation and failure of rubberlike materials, J. Mech. Phys. Solids 122 (2019) 538–554.

[57] F. Stadlbauer, T. Koch, V.M. Archodoulaki, F. Planitzer, W. Fidi, A. Holzner, Influence of experimental parameters on fatigue crack growth and heat build-up in rubber, Materials 6 (12) (2013) 5502–5516.

[58] A.N. Gent, Engineering with Rubber: How to Design Rubber Components, third ed., Hanser Publishers, 2012.

[59] J. Bonet, R.D. Wood, Nonlinear Continuum Mechanics for Finite Element Analysis, Cambridge University Press, 2008.

[60] A. Cristiano, A. Marcellan, R. Long, C.-Y. Hui, J. Stolk, C. Creton, An experimental investigation of fracture by cavitation of model elastomeric networks, J. Polym. Sci. B 48 (2010) 1409–1422.

[61] A. Zine, N. Benseddiq, M. Naït Abdelaziz, Rubber fatigue life under multiaxial loading: Numerical and experimental investigations, Int. J. Fatigue 33 (10) (2011) 1360–1368.

[62] P.L. Rosendahl, M. Drass, J. Felger, J. Schneider, W. Becker, Equivalent strain failure criterion for multiaxially loaded incompressible hyperelastic elastomers, Int. J. Solids Struct. 166 (2019) 32–46.

[63] M. Fassin, R. Eggersmann, S. Wulfinghoff, S. Reese, Efficient algorithmic incorporation of tension compression asymmetry into an anisotropic damage model, Comput. Methods Appl. Mech. Engrg. 354 (2019) 932–962.

[64] J.Y. Wu, V.P. Nguyen, H. Zhou, Y. Huang, A variationally consistent phase-field anisotropic damage model for fracture, Comput. Methods Appl. Mech. Engrg. 358 (2020).

[65] H. Amor, J.J. Marigo, C. Maurini, Regularized formulation of the variational brittle fracture with unilateral contact: Numerical experiments, J. Mech. Phys. Solids 57 (8) (2009) 1209–1229.

[66] G.A. Holzapfel, Nonlinear Solid Mechanics: A Continuum Approach for Engineering, second ed., John Wiley & Sons, 2001.

[67] J.Y. Wu, M. Cervera, A novel positive/negative projection in energy norm for the damage modeling of quasi-brittle solids, Int. J. Solids Struct. 139–140 (2018) 250–269.

[68] C. Steinke, M. Kaliske, A phase-field crack model based on directional stress decomposition, Comput. Mech. 63 (5) (2019) 1019–1046.

[69] H. Kiewel, J. Aktaa, D. Munz, Application of an extrapolation method in thermocyclic failure analysis, Comput. Methods Appl. Mech. Engrg. 182 (2000) 55–71.

[70] A. Abdul-Latif, D. Razafindramary, J.C. Rakotoarisoa, New hybrid cycle jump approach for predicting low-cycle fatigue behavior by a micromechanical model with the damage induced anisotropy concept, Int. J. Mech. Sci. 160 (2019) 397–411.

[71] S.V. Hainsworth, An environmental scanning electron microscopy investigation of fatigue crack initiation and propagation in elastomers, Polym. Test. 26 (1) (2007) 60–70.